LAWRENCE
LIVERMORE
NATIONAL
LABORATORY

LLNL-JRNL-650417

DEM analysis of non-coaxial flow under rotational shear

Z. Tong, P. Fu, Y. F. Dafalias, Y. Yao

February 24, 2014

International Journal for Numerical and Analytical Methods in Geomechanics

Disclaimer

DEM analysis of non-coaxial flow under rotational shear

Zhaoxia Tong[1], Pengcheng Fu[2], Yannis F. Dafalias[3](M.ASCE), and Yangping Yao[4*]

[1]Assistant Professor, School of Transportation Science and Engineering, Beihang University, Beijing 100191, China. E-mail: tongzx@buaa.edu.cn

[2]Research Scientist, Atmospheric, Earth, and Energy Division, Lawrence Livermore National Laboratory, Livermore, CA 94550. Email: fu4@llnl.gov

[3]Professor, Dept. of Civil and Environmental Engineering, Univ. of California, Davis, CA 95616; and, Dept. of Mechanics, School of Applied Mathematical and Physical Sciences, National Technical Univ. of Athens, Zographou, 15773 Athens, Hellas. E-mail: jfdafalias@ucdavis.edu

[4]Professor, School of Transportation Science and Engineering, Beihang University, Beijing 100191, China (corresponding author). E-mail: ypyao@buaa.edu.cn

Abstract:

This study focuses on non-coaxial flow behavior of cohesionless soil undergoing cyclic rotational shear, with a special interest in the effects of particle-scale characteristics. To this end, we perform a series of 2D discrete element simulations with various particle shapes, inter-particle coefficient of friction, initial density, and stress ratios. The validity and efficacy of the numerical model is established by systematically comparing numerical simulation results with existing laboratory testing results. Such comparison shows that the numerical simulations are capable of capturing mechanical behavior observed in laboratory testing under rotational shear. We further demonstrate and quantify a strong yet simple relationship between the deviatoric part of the normalized strain increment and the non-coaxial angle, denoted by $(\Delta\varepsilon)_{\mathrm{q}}^{R}$ and ψ respectively. This quantitative correlation between ψ and $(\Delta\varepsilon)_{\mathrm{q}}^{R}$ is independent of applied stress ratio, initial and current void ratio, and the number of cycles applied, but dependent on the principal stress orientation and particle-scale characteristics. At the same $(\Delta\varepsilon)_{\mathrm{q}}^{R}$, specimens with higher inter-particle friction angle or smaller particle aspect ratio show greater non-coaxial angles. A simple model $\psi = 45^{\mathrm{o}} m^{(\Delta\varepsilon)_{\mathrm{q}}^{R}}$ is able to fit this ψ - $(\Delta\varepsilon)_{\mathrm{q}}^{R}$ relationship well, which provides a useful relationship that can be exploited in developing constitutive models for rotational shearing.

Keywords: non-coaxial flow; rotational shear; discrete element method; anisotropy; cohesionless soil

1 Introduction

Under certain repeated loading conditions such as earthquake, traffic, and waves, soils in geo-structures undergo not only cyclic variation of principal stress magnitudes but also rotation of principal stress axes. In some cases, cyclic stress rotation is the predominant feature of loading [1]. Rotation of principal stress axes with fixed principal stress values is one of the two cases named "rotational shear" by Wang et al. [2]; the other case is the variation of principal stress values with fixed stress axes such that the stress orbit in π-plane is circular. In both cases the second deviatoric stress invariant J is fixed. Henceforth in the current paper, rotational shear will refer to rotation of principal stress axes with fixed principal stresses.

Two aspects of soil behavior under rotational shear have received much attention in previous studies: the accumulation of volumetric strain and the non-coaxiality between the directions of stain increment and stress. In terms of volumetric change under rotational shear, existing laboratory test results unanimously indicated that contractive volumetric strain tends to accumulate progressively [3-8]. Under undrained conditions, this tendency results in positive pore pressure and even liquefaction [1, 9-13]. On the other hand, the flow rule, which specifies the relationship between the magnitude and direction of plastic strain increment and those of the stress tensor, is an important component of the theory of plasticity. Significant non-coaxiality, namely the deviation of the plastic strain increment direction from stress direction, has been observed for loading conditions involving stress rotation [1, 3-4, 8, 10, 14-19]. Through simple shear tests, where limited monotonic rotation of principal stress axes can be achieved, Roscoe et al. [14] discovered that directions of strain increment and stress are not coincident, particularly at the early stage of loading. Wong and Arthur [15] conducted continuous stress rotation tests on Standard Leighton Buzzard sand using a directional shear cell. The test results revealed that the strain increment direction is controlled by the direction of stress increment instead of that of stress. Due to its ability to achieve arbitrary stress orientations, hollow cylinder apparatus (HCA) has become an indispensable tool for studying stress rotation. Using HCA, tests under purely stress rotation condition, namely rotational shear, has been conducted by many researchers [3-8, 18]. In the tests conducted by Symes et al. [4] using medium-loose Ham River sand, it was found that the non-coaxial angle ψ, by which the direction of strain increment precedes that of stress, is dependent on the orientation of the consolidation stress with respect to the bedding plane, and the maximum non-coaxial angle can be as large as 20°. Miura et al. [3], Tong et al. [8], and Gutierrez et al. [18] have all tested Toyoura sand in their respective studies. Non-coaxial angles exceeding 30° were observed by Miura et al. [3] and Tong et al. [8]. Gutierrez et al. [18] carried out three kinds of stress paths on Toyoura sand and found that the non-coaxial angle ψ for loadings involving stress rotation is much greater than that without stress rotation. Gutierrez et al. [18] also found that non-coaxial angle ψ decreases with the increase of shear stress level. The direction of strain increment and that of stress tend to become coincident as the stress state approaches failure. Various stress paths were tested by Cai et al. [19] on Portaway sand and Leighton Buzzard sand to investigate the effects of soil density, deviatoric stress, and material anisotropy on non-coaxial flow behavior. They found that the sand type and density affect non-coaxiality, and the effects are more significant at lower shear stress level. The effects of shear stress level on non-coaxial angle ψ are consistent with that observed by Gutierrez et al. [18]. Simulation of rotational shear response by macroscopic constitutive modeling has been addressed by many works, and here suffices to mention the one by Wang et al. [2] where the term rotational shear was introduced.

The primary objective of the current study is to explore the effects of particle-scale characteristics, including particle shapes and inter-particle coefficient of friction, on cohesionless soil's non-coaxial flow behavior under rotational shear, with a special focus on the manifestation of fabric anisotropy. The understanding of these effects plays an essential role in establishing advanced constitutive models based on particle-scale physics [20-22]. Each one of the aforementioned experimental studies in the literature used a specific type of natural sand, and it is extremely difficult, if at all possible, to isolate variables characterizing soil particles in such laboratory experiments. Therefore, the current study uses virtual sands simulated with the discrete element method (DEM) [23], where these particle-scale variables can be independently controlled in a convenient fashion. DEM simulation has been used in numerous studies concerning monotonic loading conditions such as the biaxial/triaxial compression tests [e.g. 24-27] and direct/simple shear tests [e.g. 27-30], and proved its efficacy in the study of soil behaviors. However, DEM studies under rotational shear are relatively rare. A particularly noteworthy advancement in this front was made by Li and Yu [31], where they found that the non-coaxiality in rotational shear was produced due to the rotation of internal material structure.

The current paper is organized as follows: Section 2 presents the numerical methods used in this study and the factorial design of the simulations. General behavior of the virtual sand under cyclic stress rotation is discussed in section 3. The validity and efficacy of the numerical method is established by comparing such behavior with its counterpart phenomenon observed in real world experiments. In section 4, we investigate the non-coaxial flow behavior including the effects of stress ratio, initial void ratio, inter-particle friction angle, and particle aspect ratio. We also continue to compare numerical simulation results with their laboratory experiment counterparts whenever applicable to reassure the validity of the former. Observations and conclusions are summarized in section 5.

2 Implementation of Numerical Experiments

2.1 The DEM model

The current study uses a 2D discrete element code, PPDEM [32], as the simulation and analysis platform. The polyarc element in PPDEM can represent arbitrary 2D particle shapes by replacing the straight edges in more conventional polygon elements (e.g. [33-36]) with circular arcs of various radii of curvature. Elliptical particles with different aspect ratios are employed in the current study. Each elliptical particle shape is approximated with a polyarc with four curved edges, which is a well-established practice with a long history [37]. Figure 1 illustrates polyarc particles used in the current study. Two particles i and j are considered to be in contact when their geometrical profiles overlap. The "contact law" determines the normal and tangential interaction forces, denoted by F_n and F_s respectively, between the two particles as

$$F_n = K_n A_{ij} \qquad (1)$$

$$\Delta F_s = K_s l_{ij} v_t \Delta t \qquad (2)$$

where K_n is the normal contact stiffness; A_{ij} is the overlap area between the profiles of the two particles; ΔF_s is the incremental shear force from the previous time step to the current time step; K_s is the shear contact stiffness; l_{ij} is the length between the two intersection points between the two particles' profiles; v_t

is the relative tangential velocity between the two particles at the contact point; and Δt is the time increment size. The shear contact force is expressed in an incremental form to facilitate the enforcement of Coulomb's criterion $F_s \leq F_n \tan\phi_{pp}$, where $\tan\phi_{pp}$ is the inter-particle coefficient of friction. In the current study, $K_n = 2.15 \times 10^{12}$ N/m^2 and $K_s = 7.16 \times 10^{11}$ N/m^2. Other algorithmic aspects of PPDEM are described in Fu et al. [32] in detail and not repeated here. PPDEM has been successfully applied in a number of studies [21, 27, 38-39] with comparable parameters to those used in the present paper. Therefore, all these studies, including the current one, can be considered to have used the same or similar "virtual materials". It should be noted that this simulation platform has been used especially in revealing soil behavior rooted in inherent fabric anisotropy. Past applications revealed previous unknown soil behavior [27] in terms of strength anisotropy, which was later validated by laboratory experiment [40].

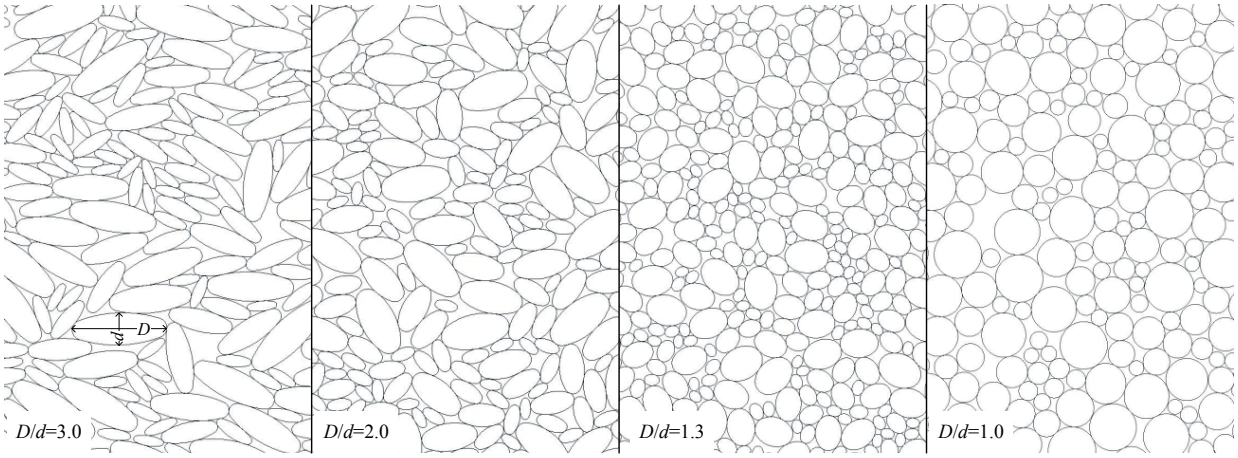

Figure 1 Virtual specimens (magnified view) consisting of elliptical particles with different aspect ratios (D/d) used in the current study.

2.2 Factorial Design of Numerical Experiments

The variables investigated in the study include particle aspect ratio (D/d), the inter-particle friction angle (ϕ_{pp}), initial void ratio (e_0) prior to the rotation of stress axes, and the stress ratio $R=(\sigma_1-\sigma_3)/(\sigma_1+\sigma_3)$, where σ_1 and σ_3 are the two principal stress components in 2D. Each virtual particle assembly consists of elliptical particles with the same aspect ratio but different sizes. Four aspect ratios, namely 3.0, 2.0, 1.3 and 1.0 (circular disks) are included. In each assembly, the largest particle is 3.33 times larger than the smallest in terms of the major axis length (D), and particle sizes are randomly distributed between the upper and lower limits. The areas (equivalent to volume in 3D) of the particles are the same across all assemblies. Therefore, the ranges of particle major axis lengths are 0.30 to 1.0 mm, 0.24 to 0.82 mm, 0.20 to 0.67 mm, and 0.17 to 0.58 mm, respectively, for the four aspect ratios. The mean stress p is a constant, 200kPa, for all simulations. The stress ratio varies within the range that does not cause excess or unstable deformation of the specimens, so the highest stress ratio used varies slightly from specimen to specimen. Generally, specimens with smaller initial void ratio and higher inter-particle friction angle can withstand higher stress ratios. Because of the high consistency in the trends observed in the simulation results, we

found the fractional factorial design as shown in Table 1 to be sufficient for revealing the effects of these variables. Each specimen is subjected to at least 22 cycles of rotational shear. Note that due to the 2-fold rotational symmetry of stress axis rotation, a "cycle" refers to a clockwise rotation of the principal axes of the stress tensor by 180 degrees.

Table 1 Experiment factorial design

Label	Particle aspect ratio	Inter-particle friction angle ϕ_{pp}	Void ratio before rotation[a] e_0	Stress ratio R applied $R=(\sigma_1-\sigma_3)/(\sigma_1+\sigma_3)$
AR30ϕ35	3.0	35°	0.275	0.05/0.10/0.15/0.20/0.25/0.30
			0.251	0.10/0.15/0.20/0.25/0.30/0.35
			0.235	0.30
			0.210	0.30
AR30ϕ27	3.0	27°	0.221	0.10/0.20/0.30/0.35
AR30ϕ20	3.0	20°	0.192	0.10/0.20/0.30
AR20ϕ35	2.0	35°	0.211	0.10/0.20/0.30/0.35
AR13ϕ35	1.3	35°	0.212	0.10/0.20/0.25
AR10ϕ35	1.0	35°	0.210	0.10/0.20/0.25

Note: [a]The initial void ratio is slightly (within ±0.001) affected by the applied stress ratio. Shown in the table are the average values for different stress ratios.

2.3 Sample Preparation

The specimen fabrication process is similar to that presented in Fu and Dafalias [27]. First, a loose pack containing 20,000 ellipse-shaped or disk-shaped particles is generated. The particles are then pluviated into a box, forming a natural fabric by simulating the particle deposition process under natural gravity. After the particles settle in the box, a circular specimen for the rotational shear tests is 'trimmed' as shown in Figure 2(a). The desired consolidation stress is then directly applied to the exterior of the specimen. Because this applied external stress is different from the internal stress resulting from the deposition, the specimen is not in equilibrium. We temporarily use a high viscous damping factor to maintain the stability of the system, and gradually reduce the damping as equilibrium is reached. Therefore the consolidation stress path is not rigorously controlled. For significantly elongated particles, the inherent fabric anisotropy locked in the specimen during the deposition is much stronger than the anisotropy induced by the anisotropic consolidation stress. The consolidation stress path is unlikely to have a

significant effect on the results of the current study. Approximately 6,000 particles are included in each 'trimmed' specimen and the radii of the trimmed specimens are typically in the vicinity of 15 mm. We also performed simulations with larger specimens of 12,000 particles and found that the results are practically identical to those of the 6,000-particle specimens, proving that the specimen dimension chosen is adequate for obtaining statistically representative results.

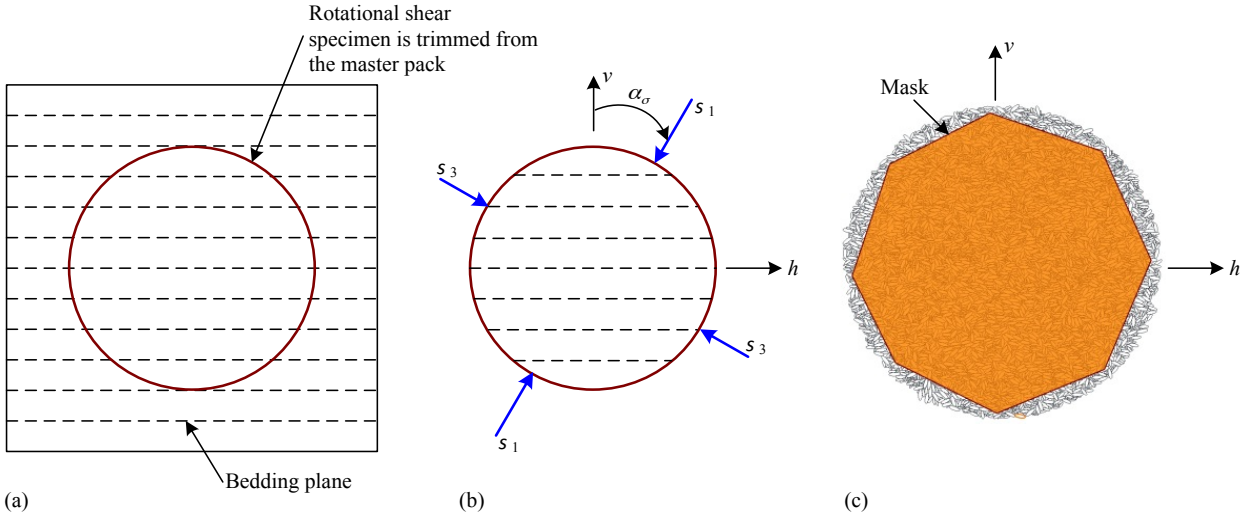

Figure 2 Specimen fabrication, loading, and mask definition: (a) trim of the specimen from the master pack; (b) schematic view of the applied rotational stress and the definition of the major principal stress direction α_{σ}; and (c) illustration of the "mask" for stress and strain measurement.

2.4 Application of Rotational Shear Loading

In real world HCA apparatus, normal stress in the vertical direction and shear stress are applied through servo-controlled rigid boundaries (the upper and lower rings). The hoop stress is controlled by the differential pressure between the inner and outer chambers. In previous studies [31] using 2D DEM to simulate rotational stress conditions, stresses were also applied through servo-controlled kinematic boundaries. The current study uses a novel method to achieve arbitrary stress states without the use of kinematic constraints, so that the specimen can freely deform and the homogeneity of the applied stress is guaranteed. In this method, forces along the principal stress directions are directly applied to boundary particles as shown in Figure 3, and the boundary particles are automatically identified during loading. The efficacy of this method will be proved in Section 3.1 by comparing the stress values calculated based on internal force chains and the specified stress.

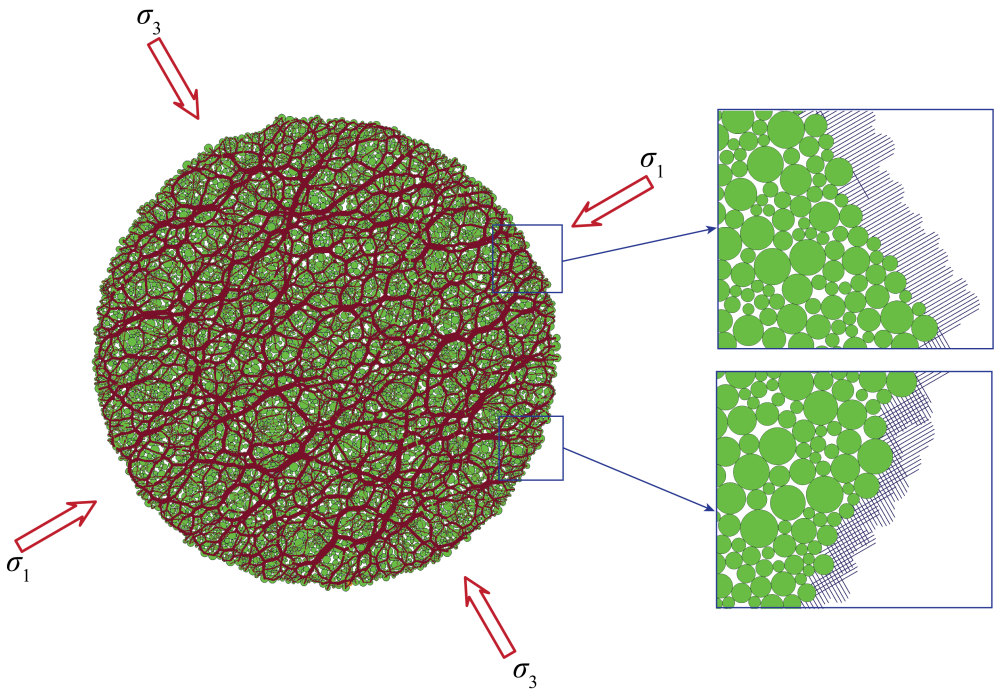

Figure 3 A conceptual illustration of the special method of applying arbitrary stresses to DEM specimen boundary without kinematic constraints. The force chains inside the specimen are shown. In the two magnified views, the thin blue lines annotate the forces applied to boundary particles along the principal stress directions.

In a simulation, the 'trimmed' circular specimen is consolidated anisotropically to the specified stress state. During consolidation, the major principal stress σ_1 is applied along the vertical deposition direction (v-axis) and the minor principal stress σ_3 is along the horizontal direction (h-axis). The direction of major principal stress, defined as the clockwise angle α_σ between the deposition direction and the direction of σ_1, is zero during this process. The cyclic rotational shearing begins after the consolidation. The stress path afterwards follows the so-called 'pure rotation' condition, where the direction of major principal stress measured by α_σ rotates clockwise continuously while the magnitudes of the principal stresses (σ_1 and σ_3) remain constant, i.e. the definition of rotational shear. Therefore, the measured deformation of the specimen is caused by the variation of α_σ alone.

2.5 Measurement of Stress and Strain Parameters

In the analysis of DEM simulation results, stresses and strains are calculated based on grain-scale quantities in a statistical sense. This is because the strict definitions of both stress and strain are based on the assumption of continuum, which is only applicable for granular materials at length scales much larger than particle sizes in a homogenized sense. The homogenized stress tensor $\overline{\sigma}_{ij}$ in a given granular particle assembly can be calculated as

$$\bar{\sigma}_{ij} = \frac{1}{S}\sum_{c\in S} f_i^c l_j^c \qquad (3)$$

where $\bar{\sigma}_{ij}$ is the ij component of the average stress; S is the volume (area in 2D) of the assembly; c is an index that runs over all the inter-particle contact points in the assembly; f_i^c is the i component of cth contact force; and l_j^c is the j component of the contact vector (connecting the centers of the two particles in contact) of the cth contact.

Strains in a given particle assembly are calculated using the method proposed by Fu and Dafalias [38]. The state after the anisotropic consolidation is chosen as the *reference state* for strain calculation. For each specimen, over 600 reference triangles with each vertex attached to a particle are randomly generated to cover the specimen. The edges of these reference triangles are approximately 2.5 mm long, and the triangles deform along with the movements of the three particles that it is attached to. Figure 4 illustrates a reference triangle in an elliptical particle assembly.

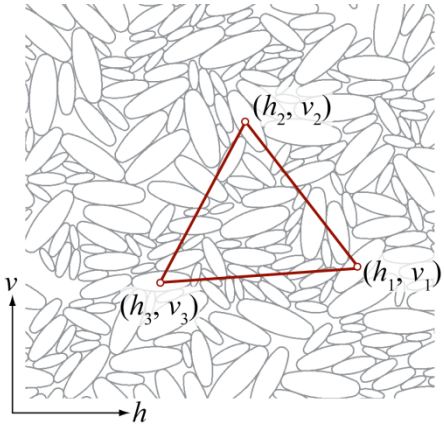

Figure 4 A reference triangle attached to three particles for strain calculation.

The strain for each reference triangle is calculated based on the deformation as

$$\begin{bmatrix}\varepsilon_{hh}\\ \varepsilon_{hv}\\ \varepsilon_{vv}\end{bmatrix} = \frac{1}{2A}\begin{bmatrix} v_2-v_3 & 0 & v_3-v_1 & 0 & v_1-v_2 & 0\\ h_3-h_2 & v_2-v_3 & h_1-h_3 & v_3-v_1 & h_2-h_1 & v_1-v_2\\ 0 & h_3-h_2 & 0 & h_1-h_3 & 0 & h_2-h_1\end{bmatrix}\begin{bmatrix}\Delta h_1\\ \Delta v_1\\ \Delta h_2\\ \Delta v_2\\ \Delta h_3\\ \Delta v_3\end{bmatrix} \qquad (4)$$

where ε_{hh}, ε_{hv}, and ε_{vv} are the three strain components; v_i and h_i are the reference location coordinates of the ith vertex of the triangle; Δv_i and Δh_i are the displacement components of the ith vertex relative to its reference state; and A is the area of the reference triangle. Note that ε_{hv} is the engineering shear strain. The sign of normal strain components is reversed (contraction is positive) in the rest of the paper to comply with conventions of geomechanics. The homogenized strain of the specimen is the weighted (by the sizes of reference triangles) average value of strains calculated for all the overlapping reference triangles.

Because the stress-controlled boundary condition imposes no kinematic constraints to particle movement and specimen deformation, excess deformation along specimen boundary occasionally takes place during the simulation, but it only affects the deformation of a very thin layer near the surface. Following the method developed by Fu and Dafalias [21] to isolate deformation of a specific area from the rest of the specimen, we employ a polygon-shaped "mask" to cover the center part (approximately 5,000 particles) as shown in Figure 2(c). Each vertex of the mask is attached to a particle, so the mask deforms with the specimen. All the stresses and strains reported in the current paper are only calculated inside this mask. Table 2 shows the definition of the variables commonly used in the analysis of mechanical responses under the rotational shear.

Table 2 Variables commonly used under rotational shear

Stress-related variables	Stress components	σ_{hh}, σ_{vv}, and σ_{vh}
	Major and minor principal stresses	$\sigma_{1,3} = \frac{\sigma_{vv} + \sigma_{hh}}{2} \pm \sqrt{\left(\frac{\sigma_{vv} - \sigma_{hh}}{2}\right)^2 + \sigma_{hv}^2}$
	Mean stress	$p = (\sigma_1 + \sigma_3)/2$ (2D) $= (\sigma_1 + \sigma_2 + \sigma_3)/3$ (3D)
	Stress ratio	$R = (\sigma_1 - \sigma_3)/(\sigma_1 + \sigma_3)$
	Major principal stress orientation relative to the vertical axis	$\alpha_\sigma = \frac{1}{2}\arctan^{-1}\frac{2\sigma_{hv}}{\sigma_{vv} - \sigma_{hh}}$
	Increment of major principal stress orientation	$\Delta\alpha_\sigma$
	Increment of stress components	$\Delta\sigma_{hh}$, $\Delta\sigma_{vv}$, and $\Delta\sigma_{vh}$
	Major principal stress increment orientation	$\alpha_{\Delta\sigma} = \frac{1}{2}\arctan^{-1}\frac{2\Delta\sigma_{hv}}{\Delta\sigma_{vv} - \Delta\sigma_{hh}}$
Strain-related variables	Strain components	ε_{hh}, ε_{vv}, and ε_{vh}
	Volumetric strain	$\varepsilon_{vol} = \varepsilon_{hh} + \varepsilon_{vv}$
	Increment of strain components	$\Delta\varepsilon_{hh}$, $\Delta\varepsilon_{vv}$, and $\Delta\varepsilon_{vh}$
	Increment of strain components normalized by the amount of stress rotation	$\Delta\varepsilon_{hh}^R = \Delta\varepsilon_{hh}/\Delta\alpha_\sigma$, $\Delta\varepsilon_{vv}^R = \Delta\varepsilon_{vv}/\Delta\alpha_\sigma$, and $\Delta\varepsilon_{vh}^R = \Delta\varepsilon_{vh}/\Delta\alpha_\sigma$
	Deviatoric part of the normalized stress increment	$(\Delta\varepsilon)_q^R = \sqrt{\left(\Delta\varepsilon_{vv}^R - \Delta\varepsilon_{hh}^R\right)^2/4 + \left(\Delta\varepsilon_{hv}^R\right)^2}$
	Major principal strain increment orientation	$\alpha_{\Delta\varepsilon} = \frac{1}{2}\arctan^{-1}\frac{2\Delta\varepsilon_{hv}}{\Delta\varepsilon_{vv} - \Delta\varepsilon_{hh}}$
	Non-coaxial angle	$\psi = \alpha_{\Delta\varepsilon} - \alpha_\sigma$

2.6 2D vs. 3D stress paths

The numerical simulation in the current paper is based on a two-dimensional (2D) DEM model whereas the real world is a 3D space. It is well known that certain phenomena in real materials cannot be reflected by 2D models. For instance, typical void ratio values and coordination numbers in 2D particle assemblies are much smaller than those in 3D granular materials. Particularly relevant to this study, in real hollow

cylinder tests it is typically the major and minor principal stresses that are rotating; the magnitude of the intermediate stress can be independently controlled but its direction is usually fixed. The magnitude of the intermediate stress relative to that of the other two principal components was found to have a significant effect on sands' behavior under rotational shear [7-8]. On the other hand, only two principal stresses exist for 2D models and the intermediate principal stress does not apply. The readers are advised to interpret and generalize 2D simulation results with careful consideration of these factors. Nevertheless, 2D models have proved their efficacy in studying many phenomena of real materials, including in our previous work [27, 40]. The extensive comparison between 2D simulation results and their 3D real world counterparts in subsequent sections also proves this notion.

3 Validating the Numerical Results via Simulation-Experiment Comparison

In this section, we present representative numerical simulation results and compare them with their real world counterparts from laboratory experiments available in the literature, thereby validating the simulation methodology.

3.1 Achieved Stress Paths

We choose the numerical simulation with an initial void ratio e_0=0.251 and stress ratio R=0.3 in series AR30ϕ35 as the representative results to demonstrate some common behavior observed in the virtual experiments. Figures 5(a) to (d) show the development of three stress components (σ_{hh}, σ_{vv} and σ_{vh}), the stress path in deviatoric stress space of (σ_{vv}-σ_{hh})/2 versus σ_{vh}, the stress invariants (σ_1, σ_3 and p), and the direction of major principal stress (α_o), respectively. Note that the stress values presented are calculated with equation (3) based on particle-scale quantities. They are considered "virtual measurements" on the virtual specimens. Some small deviation from the specified values in the experiment plan is inevitable, and the magnitude of such deviation quantifies the efficacy of the special stress boundary condition described in section 2.4. The results show that the specified pure rotation condition is accomplished with high accuracy. The measured principal stress magnitude is typically within 0.5% of the specified value and the measured principal stress orientations are within 0.5 degree of the specified values.

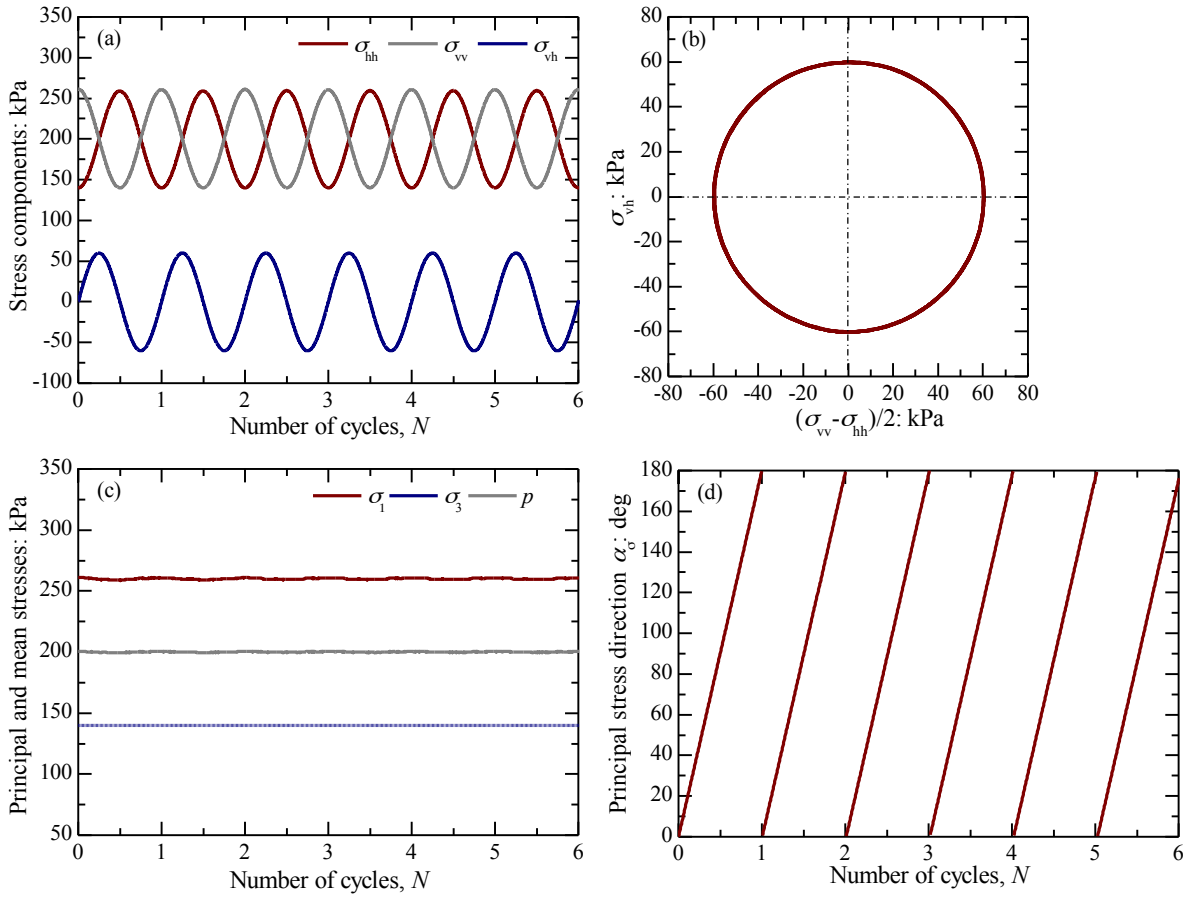

Figure 5 The achieved stress paths for the simulation with e_0=0.251 and R=0.3 in Series AR30ϕ35: (a) variation of stress components with number of cycles; (b) stress path in the space of $(\sigma_{vv}-\sigma_{hh})/2$ versus σ_{vh}; (c) variation of principal and mean stresses with number of cycles; and (d) variation of major principal stress direction with number of cycles.

3.2 Development of Strain Components

The development of strains for the same simulation is presented in Figure 6, and is compared with the HCA pure rotation test results by Zhang et al. [7] and Miura et al. [3]. Zhang et al. [7] investigated the effects of intermediate principal stress parameter b (b=(σ_2-σ_3)/(σ_1-σ_3)). We choose the test results with b=0.1 in Zhang et al. [7] to compare with our 2D simulation results, because small radial strain was produced under this condition, resembling a plane-strain state. Miura et al. [3] conducted a series of pure rotation tests under b=0.5, and this difference should be noted when comparing the results.

Figure 6(a) shows the evolution of the two normal strain components, ε_{hh} and ε_{vv}, in the numerical simulation with respect to the cycle number, and Figure 6(b) presents a magnified view within four representative cycles, namely the 1st, 2nd, 12th, and 22nd cycles. For comparison, Figures 7(a) and (b) plot test results of Zhang et al. [7] in the same fashion. Figure 8 presents the development of ε_{hh} and ε_{vv} in the first cycle obtained by Miura et al. [3], and the results from subsequent cycles are not available.

The similarity between the numerical simulation results and the laboratory experiment results is evident: Both ε_{hh} and ε_{vv} evolve periodically along with the rotational shearing. Under the pure stress rotation, the horizontal component ε_{hh} is contractive in the average of each cycle, with contractive and extensive variations within each cycle. This is partly owing to the fact that the reference state prior to stress rotation is anisotropically compressed in the vertical direction. The vertical component ε_{vv} is mostly extensive for the first few cycles. However, as the rotation continues, for higher values of N, ε_{vv} tends to contractive generation and accumulation, reflecting the overall contractive tendency of the volume change. From the magnified view, we can also see that the numerical simulation result and the counterpart laboratory data resemble each other to a high degree.

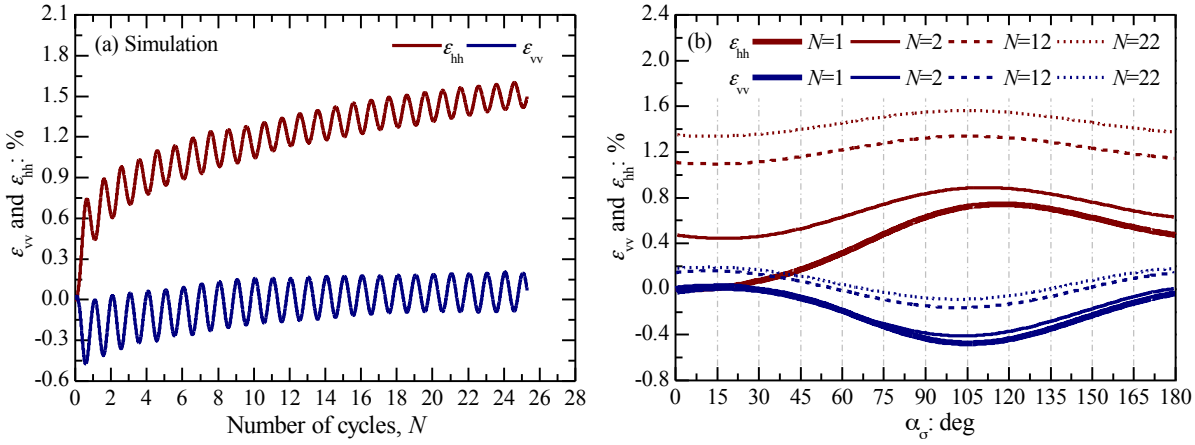

Figure 6 Variation of the two normal strain components, ε_{hh} and ε_{vv}, for numerical simulation with e_0=0.251 and R=0.3 in Series AR30ϕ35 as a function of: (a) number of cycles; and (b) major principal stress direction α_σ.

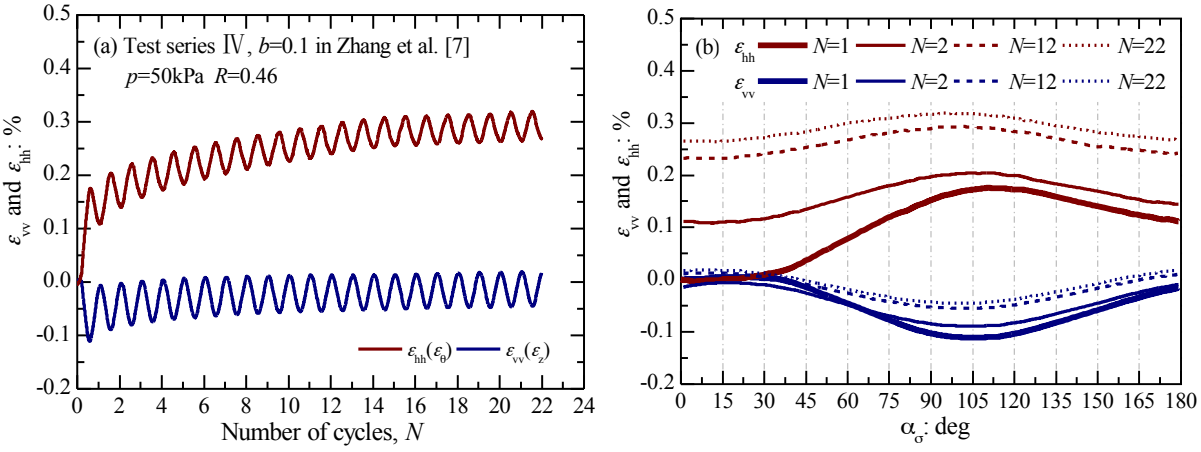

Figure 7 Variation of the two normal strain components, ε_{hh} and ε_{vv}, for test conducted by Zhang et al. [7] as a function of: (a) number of cycles; and (b) major principal stress direction α_σ.The data are extracted from Figure 6(a) of Zhang et al. [7]. The strain components of ε_z and ε_θ in Zhang et al. [7] correspond to ε_{vv} and ε_{hh} in the present work; b is the intermediate principal stress parameter.

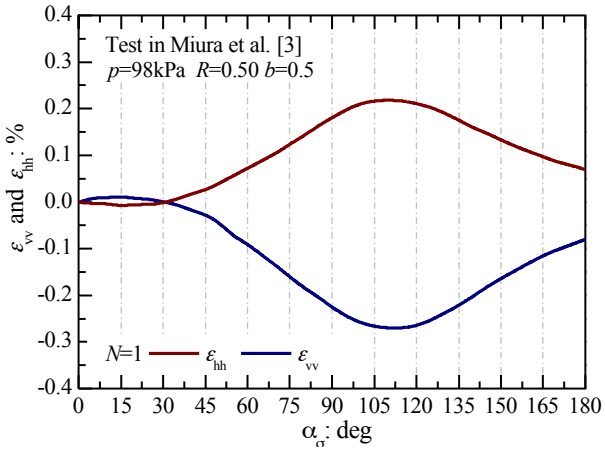

Figure 8 Variation of the two normal strain components, ε_{hh} and ε_{vv}, for test conducted by Miura et al. [3] as a function of major principal stress direction α_{σ}.The data are extracted from Figure 20(a) of Miura et al. [3]. The strain components of ε_a and ε_{θ} in Miura et al. [3] correspond to ε_{vv} and ε_{hh} in the present work; b is the intermediate principal stress parameter. Only the data for the first cycle has been reported by Miura et al. [3].

3.3 Deviatoric Strain Path

The deviatoric strain paths in the space of $(\varepsilon_{vv}-\varepsilon_{hh})/2$ versus ε_{vh} for numerical simulation and tests conducted by Zhang et al. [7] and Miura et al. [3] are presented in Figures 9(a) to (c), respectively. The deviatoric strain path in the first cycle does not constitute a closed loop. As the rotational shear continues, the deviatoric strain path gradually approaches the shape of an ellipse. Although the shapes of the paths do not exactly match between numerical results and laboratory data, the overall trends are consistent. Nevertheless, the shape of the paths is expected to be dependent on the material tested, and the virtual material is not intended to model Toyoura sand used by Zhang et al. [7] and Miura et al. [3].

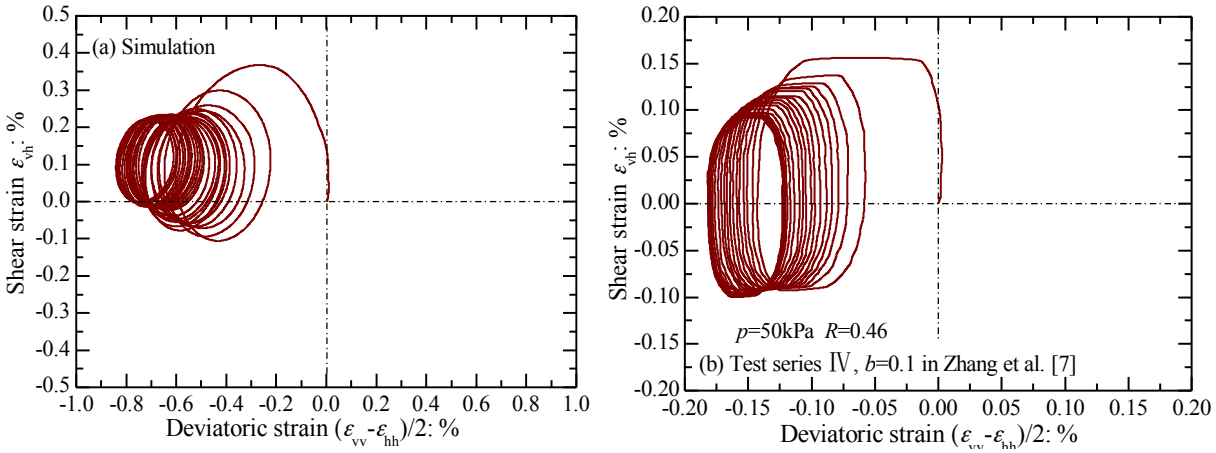

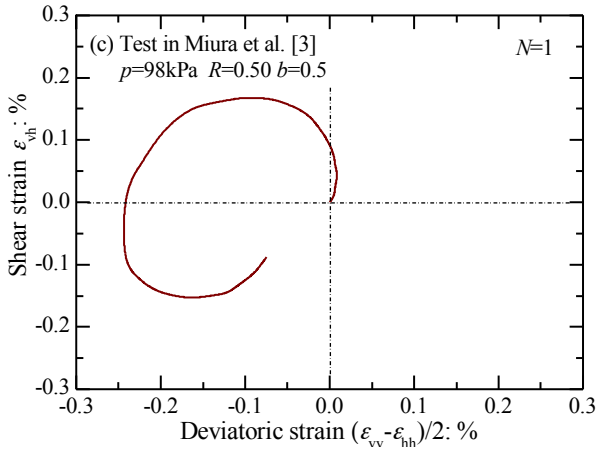

Figure 9 The deviatoric strain path in the space of $(\varepsilon_{vv}-\varepsilon_{hh})/2$ versus ε_{vh}: (a) numerical simulation with e_0=0.251 and R=0.3 in Series AR30ϕ35; (b) experimental data extracted from Figure 6(a) of Zhang et al. [7]; and (c) experimental data extracted from Figure 20(a) of Miura et al. [3]. The variables of $(\varepsilon_z-\varepsilon_0)/2$ and ε_{z0} in Zhang et al. [7], $(\varepsilon_a-\varepsilon_0)/2$ and ε_{a0} in Miura et al. [3], correspond to $(\varepsilon_{vv}-\varepsilon_{hh})/2$ and ε_{vh} in the present work; b is the intermediate principal stress parameter.

3.4 Shear Stress-Strain Relationship

Figures 10(a) to (c) present the relationships between shear stress σ_{vh} and shear strain ε_{vh} for simulation and laboratory tests. Although the curves are somewhat different in shape between simulation and laboratory results, the simulation does capture the most important characteristics of the shear stress-strain relationship. For instance, hysteretic loops are observed. As rotation continues, the double magnitude of ε_{vh}, defined as the difference between the maximum and minimum values in each single cycle, reduces due to stiffening of the specimen. Note that Zhang et al. [7] and Miura et al. [3] tested the same material (Toyoura sand), but the shapes of the the hysteric loops obtained by these two studies are also somewhat different. It is expected that factors such as specimem preparation method and test control mode can affect the shear stress-strain relationship.

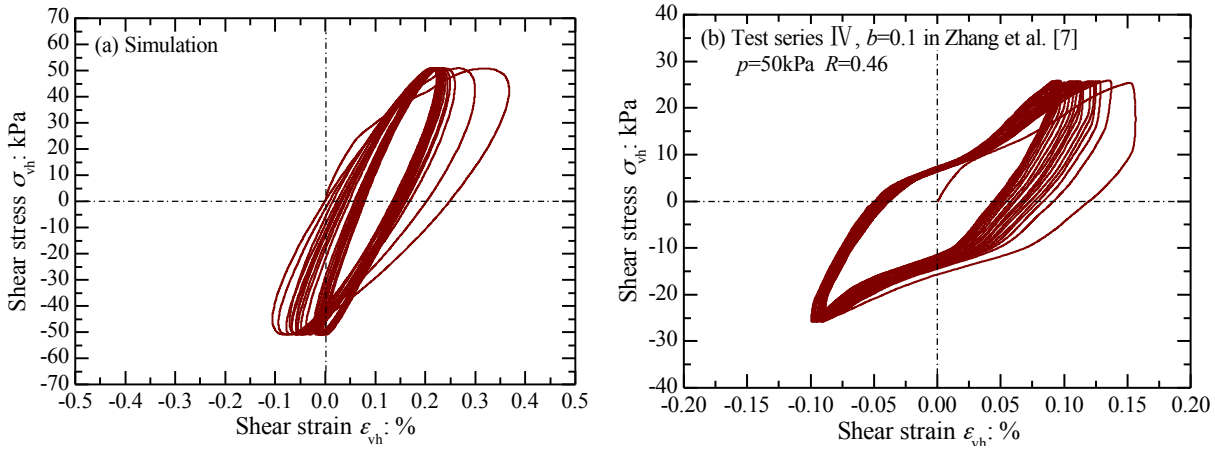

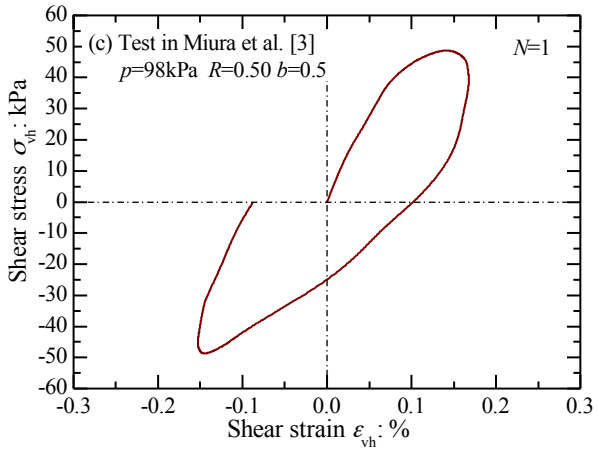

Figure 10 The relationship between shear stress σ_{vh} and shear strain ε_{vh}: (a) numerical simulation with e_0=0.251 and R=0.3 in Series AR30ϕ35; (b) test conducted by Zhang et al. [7]; and (c) experimental data extracted from Figure 20(a) of Miura et al. [3]. The variables of $\sigma_{z\theta}$ and $\varepsilon_{z\theta}$ in Zhang et al. [7], $\tau_{a\theta}$ and $\varepsilon_{a\theta}$ in Miura et al. [3], correspond to σ_{vh} and ε_{vh} in the present work; b is the intermediate principal stress parameter. The stress component σ_{vh} in the graphs (b) and (c) is calculated according to the stress condition given in Zhang et al. [7] and Miura et al. [3] respectively.

3.5 Development of Volumetric Strain

Previous laboratory experiments [3-8] have all found that cohesionless soil tends to contract under stress rotation and the contractive volumetric strain progressively accumulates as the cyclic rotation continues. Taking the simulation with e_0=0.251 and R=0.3 in Series AR30ϕ35 as an example, we plot the development of the volumetric strain ε_{vol} with the increasing number of cycles in Figure 11(a). Figure 11(b) illustrates the evolution of the volumetric strain ε_{vol} with major principal stress direction α_σ in the 1st, 2nd, 12th, and 22nd cycles. For comparison, the corresponding test results obtained by Zhang et al. [7] and Miura et al. [3] are plotted in Figures 12 and 13 respectively.

Similar behavior for the development of volumetric strain ε_{vol} is observed between numerical simulation results and laboratory tests. The specimens generally contract under stress rotation with the only exception being the small dilation observed by Miura et al. [3] in the first cycle, possibly due to the high density of the specimen in that study (82% relative density). Volumetric strain ε_{vol} shows periodical variation along with the cyclic rotation of principal stress axes. As the number of cycle increases, it accumulates progressively, while the overall rate of accumulation reduces. In the first cycle, all specimens contract when α_σ rotates from 0° to 180°. However, in subsequent cycles, the specimens dilate in the first half cycle as α_σ rotates from 0° to 90°, then followed by contraction in the later half cycle with an overall zero or very small change of volume at the end of each cycle (volume shake down).

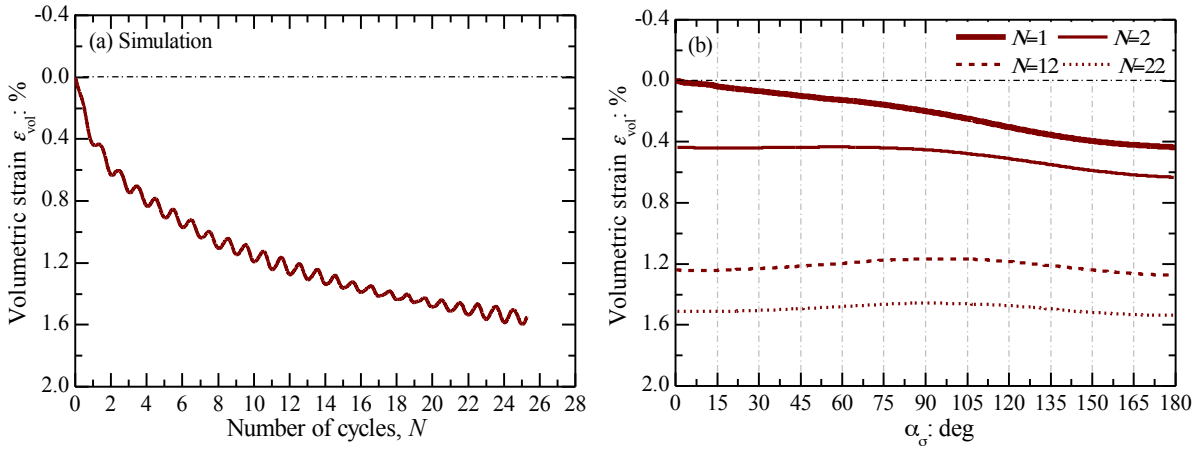

Figure 11 Variation of the volumetric strain ε_{vol} for the numerical simulation with e_0=0.251 and R=0.3 in Series AR30ϕ35 as a function of: (a) number of cycles; and (b) major principal stress direction α_σ.

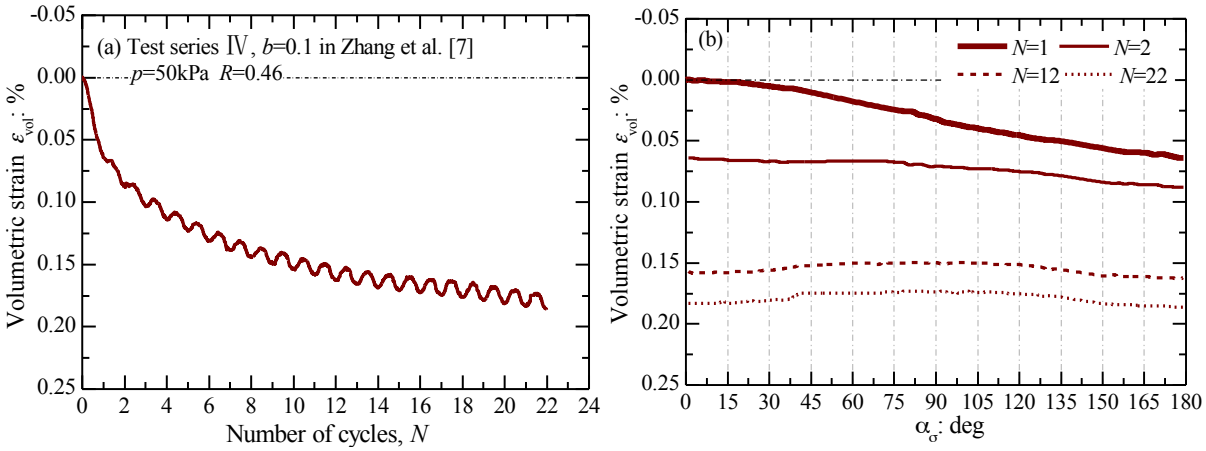

Figure 12 Variation of the volumetric strain ε_{vol} for the test conducted by Zhang et al. [7] as a function of: (a) number of cycles; and (b) major principal stress direction α_σ. The data are extracted from Figure 8(d) of Zhang et al. [7].

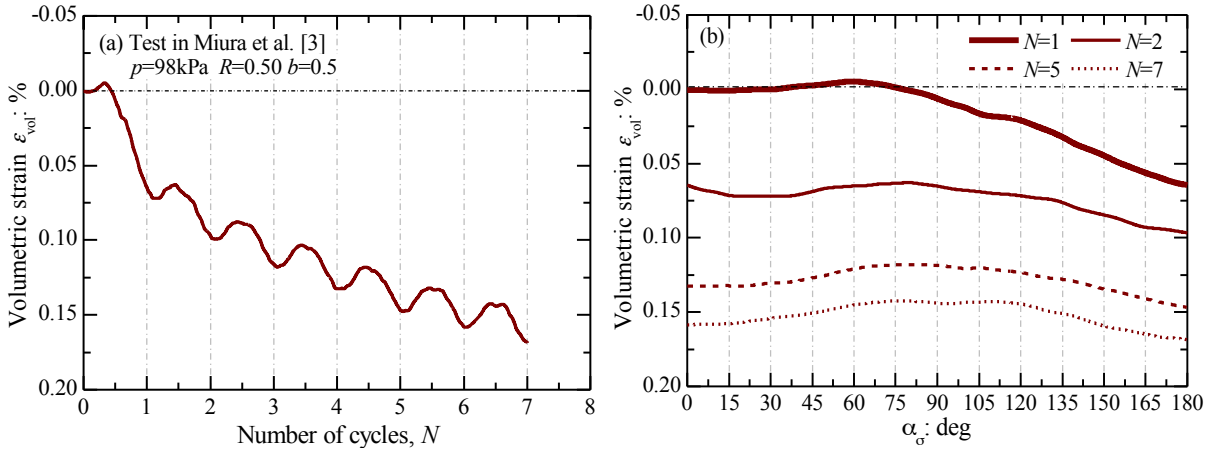

Figure 13 Variation of the volumetric strain ε_{vol} for the test conducted by Miura et al. [3] as a function of: (a) number of cycles; and (b) major principal stress direction α_{σ}. The data are extracted from Figure 28(b) of Miura et al. [3].

Through the extensive comparison between DEM simulation results in the study and the counterpart laboratory test results, we conclude that the virtual specimens resemble, to a very high degree, real world sands in mechanical behaviors in all evaluated aspects. This provides great confidence in the efficacy of the numerical model in uncovering previously unknown or unobserved mechanical phenomena as shown in the next section.

4 Non-coaxial Flow under Stress Rotation

4.1 General Observations

To formulate the flow rule under stress rotation requires knowledge of the magnitude and direction of strain increment. Figure 14 schematically shows the stress path in the plane of $(\sigma_{vv}\text{-}\sigma_{hh})/2$ versus σ_{vh} and the strain path in the plane of $(\Delta\varepsilon_{vv} - \Delta\varepsilon_{hh})/2$ versus $\Delta\varepsilon_{vh}$, where the strain increment is superposed in the corresponding stress path for easy illustration of the relationship between the strain increment direction and stress orientation. Point A denotes the current stress state; vector AB denotes the stress increment; and vector AC represents the strain increment. Under pure stress rotation, the stress increment is tangential to the stress paths in the deviatoric plane, which means that $(\alpha_{\Delta\sigma} - \alpha_{\sigma})$ is a constant 45°. The non-coaxial angle ψ is defined as the angle by which the strain increment direction precedes that of stress. It quantifies the direction of strain increment with respect to the current stress tensor orientation. In the following, we use two variables, the deviatoric part of the normalized strain increment, denoted by $(\Delta\varepsilon)_q^R$ (see Table 2 for the formulation), and the non-coaxial angle ψ, to study the flow rule under stress rotation. The variable $(\Delta\varepsilon)_q^R$ has been used in Li and Yu [31]. It should be noted that although strict plasticity theory concerns plastic strains instead of total strains, it is customary in the study of rotational shear to use total strain components [1, 3-4, 8, 10, 19]. As indicated by rotational shear test results conducted by Gutierrez et al. [18], the plastic strain increment is slightly smaller than the total strain increment at low stress level and their difference tends to diminish with the increasing stress level.

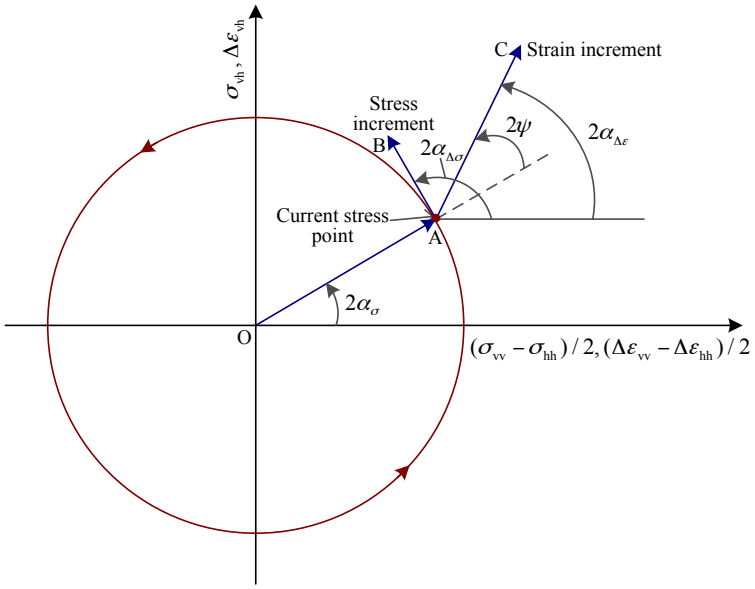

Figure 14 Illustration of stress paths and strain increment

Figures 15(a) and (b) present the development of $(\Delta\varepsilon)_q^R$ and non-coaxial angle ψ for the numerical simulation with e_0=0.251 and R=0.3 in Series AR30ϕ35. Both $(\Delta\varepsilon)_q^R$ and ψ fluctuate periodically along with stress rotation. The maximum value of $(\Delta\varepsilon)_q^R$ emerges in the first cycle, and the value of $(\Delta\varepsilon)_q^R$ tends to gradually decrease and seems to approach a 'steady' state. The development of non-coaxial angle ψ shares some certain similarity as that of $(\Delta\varepsilon)_q^R$. The minimum of ψ appears in the first cycle, and ψ tends to increase in subsequent cycles. High non-coaxial angle ψ, varied in the range of 32° to 36°, is observed when the 'steady' state is approached. The evolution trends of $(\Delta\varepsilon)_q^R$ and ψ are consistent with the results obtained by Li and Yu [31].

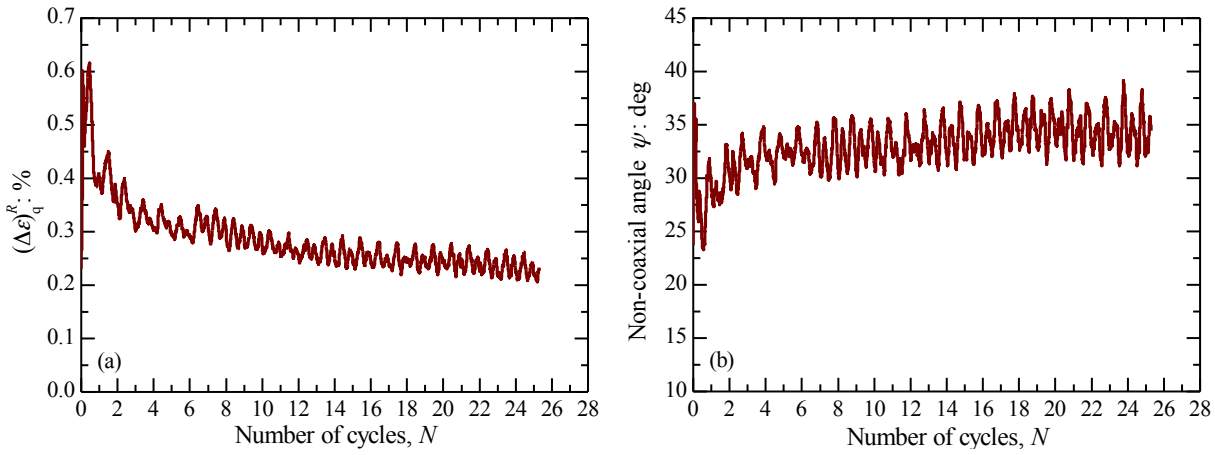

Figure 15 Development of strain increment for the simulation with e_0=0.251 and R=0.3 in Series AR30ϕ35: (a) deviatoric part $(\Delta\varepsilon)_q^R$; and (b) non-coaxial angle ψ.

In the following analysis, we demonstrate and quantify a strong yet simple relationship between the deviatoric part of the normalized strain increment and the non-coaxial angle, namely $(\Delta\varepsilon)_q^R$ and ψ under rotational shearing. As will be shown, the quantitative correlation between $(\Delta\varepsilon)_q^R$ and ψ is independent of macroscopic variables such as the shear stress ratio and void ratio, but dependent on particle-scale characteristics. Therefore, this relationship can be a useful material-dependent but state-independent "law" to explore and exploit in constitutive modeling.

4.2 Effects of Stress Level

Figures 16(a) and (b) show the development of the deviatoric part ($(\Delta\varepsilon)_q^R$) and direction (ψ) of strain increment under four different stress ratios for simulations with e_0=0.251 in Series AR30ϕ35. The effects of the stress ratio on $(\Delta\varepsilon)_q^R$ and ψ are consistent with each other. For a given stress ratio, the highest $(\Delta\varepsilon)_q^R$ value and the smallest non-coaxial angle ψ appear both in the first cycle. As the rotational shearing progresses, both $(\Delta\varepsilon)_q^R$ and ψ tend to approach 'steady' states. On the other hand, the developments of $(\Delta\varepsilon)_q^R$ and ψ are significantly dependent on the applied stress ratio. The $(\Delta\varepsilon)_q^R$ increases with the increase of stress ratio, whereas greater non-coaxial angles are generated by smaller stress ratios. The effects of stress level on $(\Delta\varepsilon)_q^R$ and ψ are consistent with the numerical simulation results presented by Li and Yu [31]. Similar effects of stress level on the non-coaxial angle ψ have been observed in the monotonic stress rotation tests conducted by Gutierrez et al. [18].

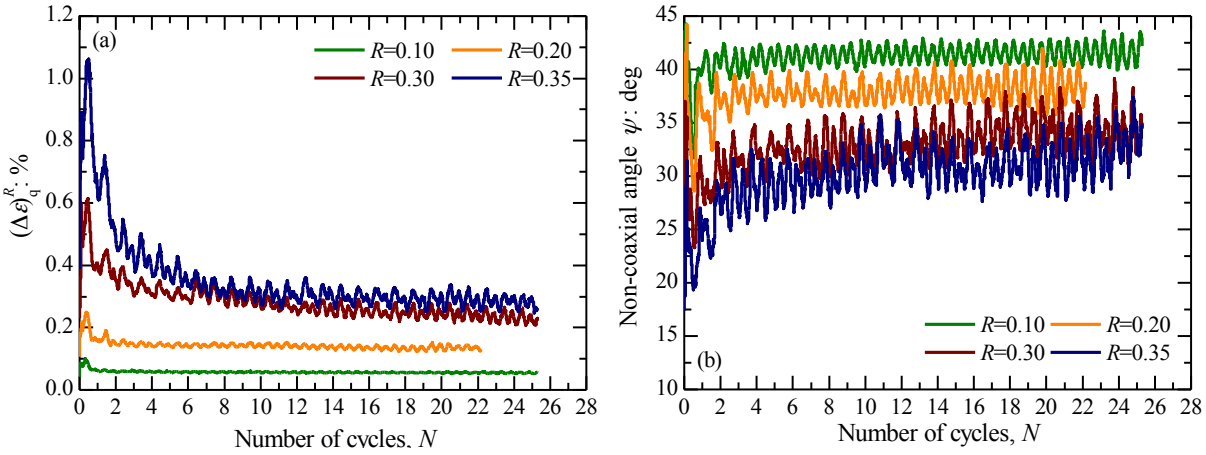

Figure 16 Development of strain increment under different stress ratios for simulations with e_0=0.251 in Series AR30ϕ35: (a) deviatoric part $(\Delta\varepsilon)_q^R$; and (b) non-coaxial angle ψ.

The relationships between $(\Delta\varepsilon)_q^R$ and ψ for specimens with e_0=0.251 in Series AR30ϕ35 are plotted in Figure 17. Data for all the six stress ratios are plotted together but denoted by different symbols. The orientation α_σ of the applied stress continuously evolves in each simulation, and the data plotted correspond to snapshots taken at four representative stress orientations, with α_σ=0°, 45°, 90°, and 135°, respectively. Note that each cycle of stress rotation generates one data points for each of the sub-figures.

For the same α_σ value, all the data points for various stress ratios and different cycles collapse into a single curve. This suggests that although the stress ratio, as an external state variable, affects the values of $(\Delta\varepsilon)_q^R$ and ψ, it has no effects on the relationship between these two quantities. On the other hand, the slope of the curve seems to be affected by the stress orientation α_σ with respect to the initial anisotropic consolidation direction. For each α_σ value, ψ decreases as $(\Delta\varepsilon)_q^R$ increases, which indicates that the direction of strain increment $\alpha_{\Delta\varepsilon}$ and that of stress α_σ tend to become coincident when the deviatoric part of the normalized strain increment $(\Delta\varepsilon)_q^R$ increases.

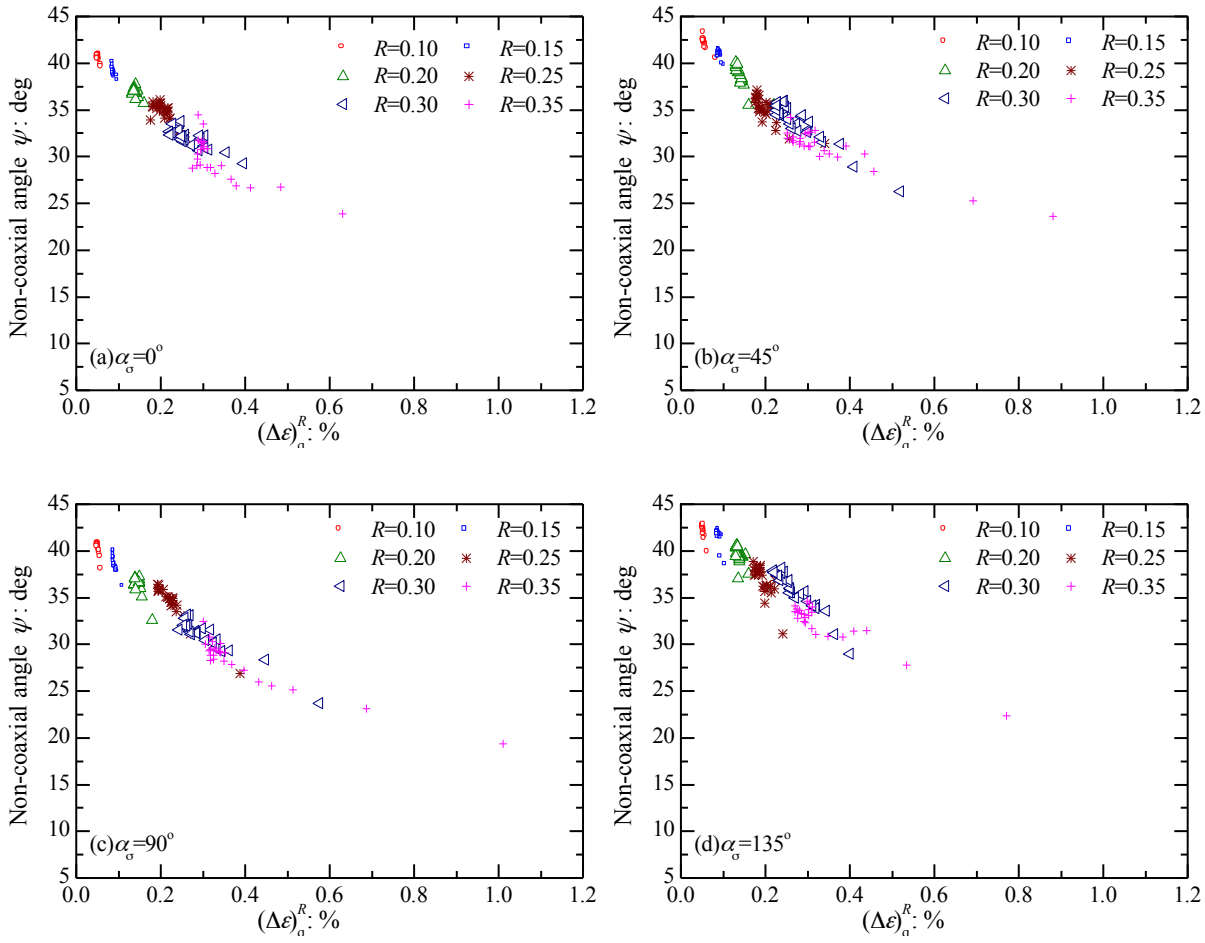

Figure 17 Relationship between ψ and $(\Delta\varepsilon)_q^R$ under different stress ratios for simulations with e_0=0.251 in Series AR30ϕ35.

4.3 Effects of Initial Void Ratio

The effects of initial void ratio on the development of $(\Delta\varepsilon)_q^R$ and non-coaxial angle ψ are presented in Figures 18(a) and (b) for the four specimens in Series AR30ϕ35 loaded with a stress ratio of R=0.3. In the first few cycles, the specimens with larger initial void ratio generally have higher $(\Delta\varepsilon)_q^R$ value and smaller

non-coaxial angle ψ. The underlying reason is likely the smaller stiffness of the looser specimens. As the cyclic rotation continues, both $(\Delta\varepsilon)_q^R$ and ψ tend to approach a 'steady' or 'semi-steady' state for the three looser specimens. The densest specimen with e_0=0.210 behaves differently: Its $(\Delta\varepsilon)_q^R$ value is lower than the semi-steady state value of the looser specimens, even from the very beginning of loading cycles. Its ψ value is higher than the 'semi-steady' state value of the looser specimens. We consider the state reached by the three loose specimens to be 'semi-steady' because the simulation data available do not definitively show whether it will continue to evolve and finally all the four specimens can reach a common steady state. This question is to be answered by future studies with a large number of cycles. Note that existing studies reported in the literature all have conducted a moderate number of rotation cycles, with up to 8 cycles in Miura et al. [3], 30 cycles in Tong et al. [8], and 60 cycles in Yang et al. [13]. Similar effects of initial void ratio on the $(\Delta\varepsilon)_q^R$ and ψ have been obtained in the numerical simulations conducted by Li and Yu [31].

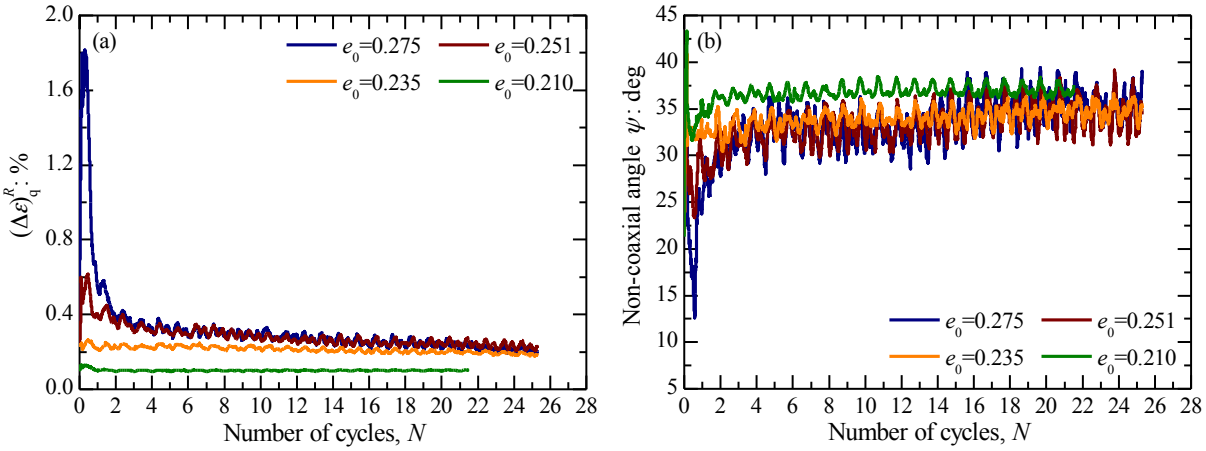

Figure 18 Development of strain increment under different initial void ratios e_0 for simulations with R=0.3 in Series AR30ϕ35: (a) deviatoric part $(\Delta\varepsilon)_q^R$; and (b) non-coaxial angle ψ.

Figures 19(a) to (d) present the correlation between the non-coaxial angle ψ and $(\Delta\varepsilon)_q^R$ at α_σ=0°, 45°, 90°, and 135° for all the 14 simulations in Series AR30ϕ35. We have demonstrated that the stress ratio R does not affect the ψ - $(\Delta\varepsilon)_q^R$ relationship, so we pool data for different stress ratios together but use various symbols to differentiate specimens with different initial void ratios. Note that void ratio evolves with rotational shearing and void ratio values at individual cycles corresponding to the data points are not explicitly represented in Figure 19. The results show that the relationship between the non-coaxial angle ψ and $(\Delta\varepsilon)_q^R$ is independent of both the initial void ratio and the current void ratio, but dependent on the α_σ value.

In order to quantify the relationship between ψ and $(\Delta\varepsilon)_q^R$, we use the simple relation to fit the data, $\psi = 45^\circ m^{(\Delta\varepsilon)_q^R}$ with m being a function of α_σ and the only unknown parameter. The simple form of the equation reflects the expected behavior of the non-coaxial angle: When $(\Delta\varepsilon)_q^R$=0, the specimen is extremely stiff and the non-coaxial angle is 45 degrees, implying coaxiality between the strain increment

and the stress increment. When $(\Delta\varepsilon)_q^R$ is very large, the strain increment is coaxial with the stress under the assumption that $m < 1$, and the specimen flows like a liquid. The corresponding fitting results by use of the foregoing power relation are shown in Figure 19 along with the scattered data points; the coefficient of determination (R^2) value is also shown. The relatively high R^2 values (between 0.77 and 0.81) indicate that the simple model fits the data well. For large $(\Delta\varepsilon)_q^R$ values, the curve significantly deviates from the data points. This is because the majority of the data points are for low $(\Delta\varepsilon)_q^R$ values, and the regression value naturally biases towards the left end of the spectrum. This deviation might also reflect the inherent inability of this extremely simple model to cover the wide range of $(\Delta\varepsilon)_q^R$ values. Despite these problems, the regression results are still reasonably good.

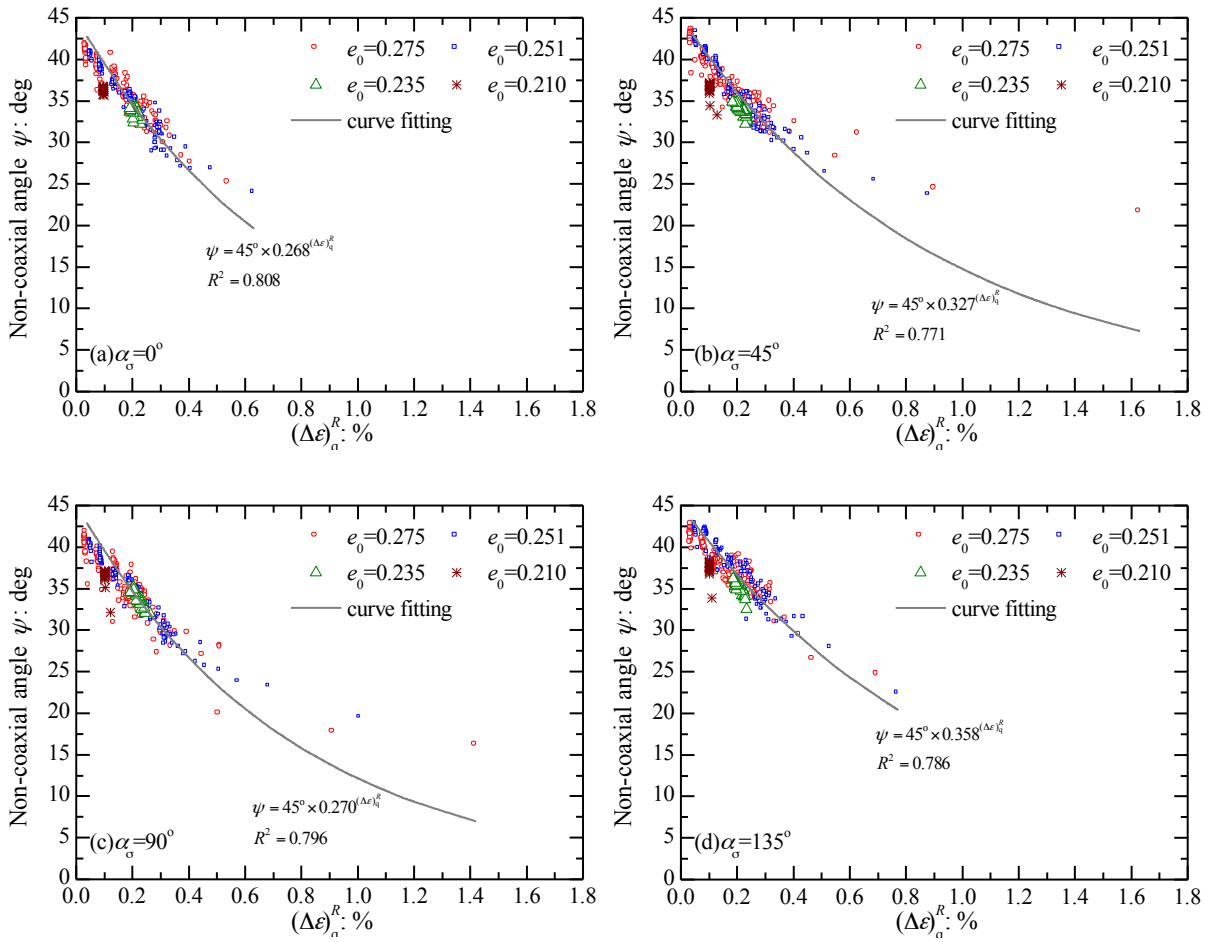

Figure 19 Relationship between ψ and $(\Delta\varepsilon)_q^R$ for all the 14 simulation results in Series AR30ϕ35.

Figure 20 shows the variations of m and R^2 with respect to α_σ for all the 14 simulation results in Series AR30ϕ35. As expected, the m value is dependent on the α_σ value, and two peaks near α_σ =45º and 135º are evident. Note that all 14 simulations are based on the same particle-scale properties, and the effects of particle-scale properties will be investigated in subsequent sections.

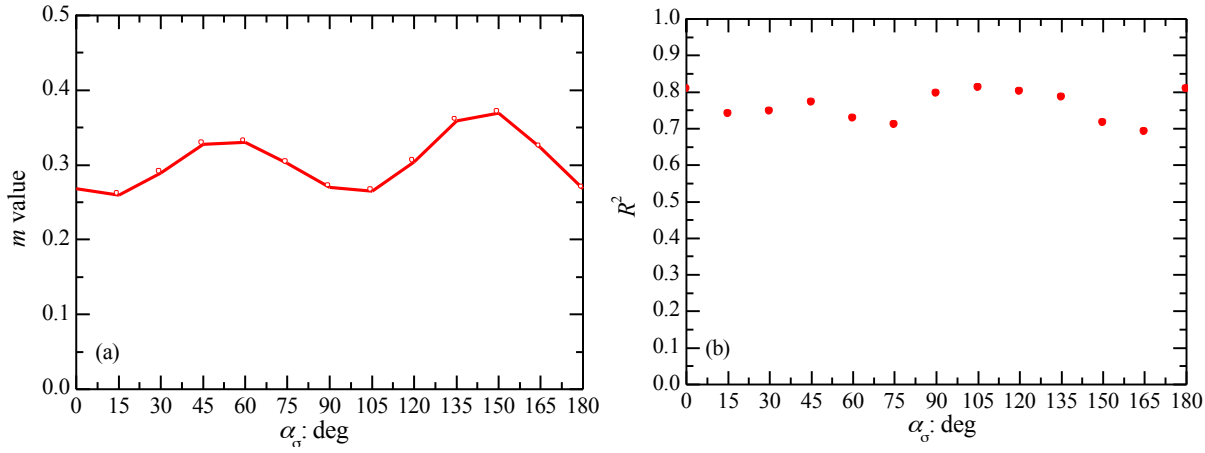

Figure 20 Parameter variation with α_σ for the curve fitting of 14 simulation results in Series AR30ϕ35: (a) m value; and (b) R^2.

4.4 Effects of Inter-particle Friction Angle

In this section, we present simulation results for virtual specimens with three different inter-particle friction angles but the same particle aspect ratio (3:1). As described in section 2.2, the three series of virtual specimens are denoted as AR30ϕ35, AR30ϕ27, and AR30ϕ20, for inter-particle friction angles ϕ_{pp} of 35°, 27°, and 20°, respectively. Figure 21 show the relationship between ψ and $(\Delta\varepsilon)_q^R$ for these three series of simulations, where data for all stress ratios simulated and all rotation cycles are pooled together. The results show that data points with the same ϕ_{pp} value collapse to a single curve for each α_σ value, and the slope of the curves is dependent on the ϕ_{pp} value: the lower the ϕ_{pp} value, the steeper the curve. This trend is evident despite of the scattering of the data points.

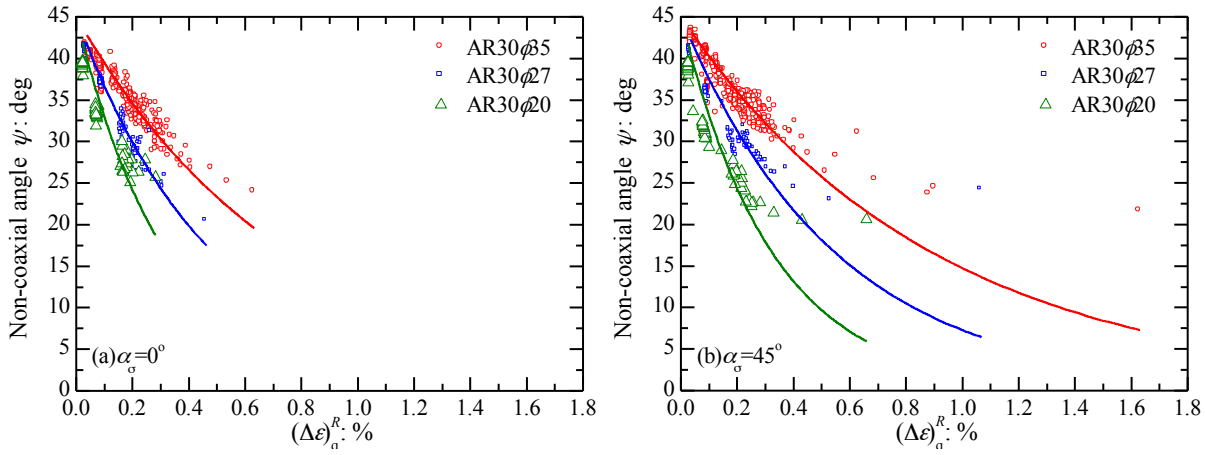

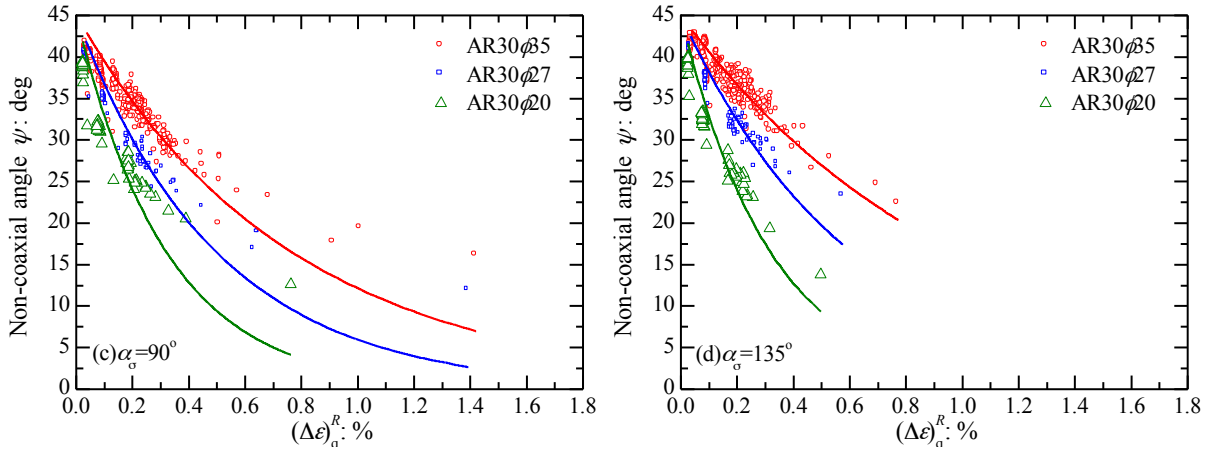

Figure 21 Effects of inter-particle friction angle on the relationship between ψ and $(\Delta\varepsilon)_q^R$.

We use the equation $\psi = 45^o m^{(\Delta\varepsilon)_q^R}$ to fit the data in Figure 21. In this context, the coefficient m is not only a function of α_σ, but also dependent on inter-particle friction angle ϕ_{pp}. The regression results are summarized in Figure 22 and show that the effects of ϕ_{pp} are two-folds: First, higher ϕ_{pp} value results in higher m value for any given α_σ. Higher m value implies less steeper ψ-$(\Delta\varepsilon)_q^R$ curve. Second, the magnitude of the variation of m with respect to α_σ increases with the increase of ϕ_{pp} value. Because such periodical variation of m reflects fabric anisotropy in the material, this observation indicates that specimens with higher inter-particle friction angle can "lock-in" stronger anisotropy in material fabric.

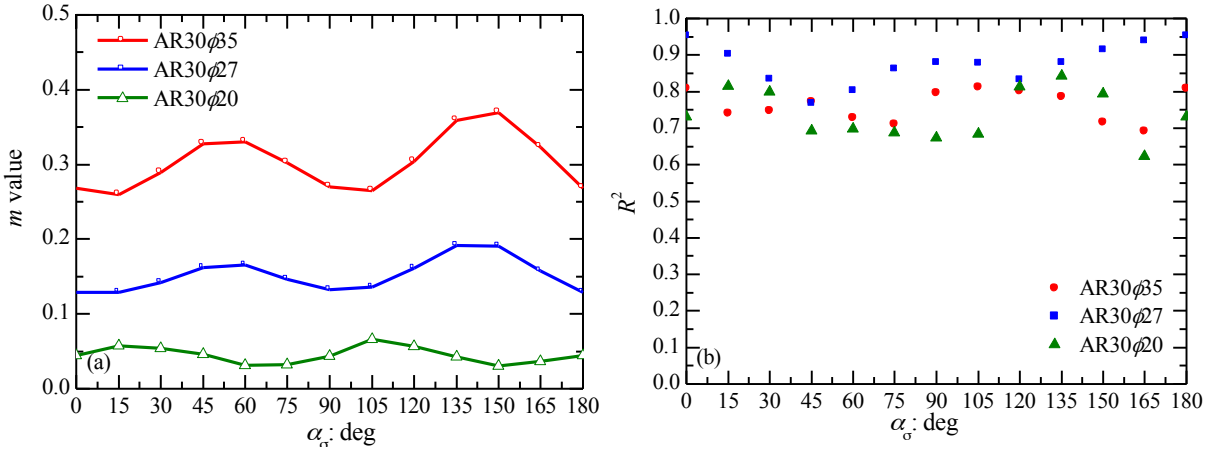

Figure 22 Effects of inter-particle friction angle on variation of: (a) m value; and (b) R^2.

4.5 Effects of Particle Aspect Ratio

Series AR30ϕ35, AR20ϕ35, AR13ϕ35, and AR10ϕ35 use the same inter-particle friction angles ϕ_{pp} of 35° but different particle aspect ratios: 3.0, 2.0, 1.3, and 1.0, respectively. Figure 23 plots the relationship between ψ and $(\Delta\varepsilon)_q^R$ at α_σ=0°, 45°, 90°, and 135° for these four series of simulations. Despite the apparent

scattering of the data points, the effects of particle aspect ratio on the relationship between ψ and $(\Delta\varepsilon)_q^R$ can be clearly discerned. The curve fitting results using equation $\psi = 45^o m^{(\Delta\varepsilon)_q^R}$ are also shown in Figure 23 and summarized in Figure 24. The model fits all the data well with the R^2 value generally higher than 0.7. According to the simulation results, specimens consisting of more elongated particles yield steeper ψ - $(\Delta\varepsilon)_q^R$ curves and thereby smaller m values. It is interesting to notice that the m values for circular disk particles are comparable with those for particles with an aspect ratio of 1.3. The magnitude of the periodical variation of m with respect to the α_σ angle seems to be modestly dependent on the aspect ratio, with more elongated particles showing more significant variation. The α_σ values where m reaches its maximum and minimum values also depend on the aspect ratio. For the specimens with elongated particles, the peak of the α_σ- m curve generally shifts rightwards as the particles become more elongated.

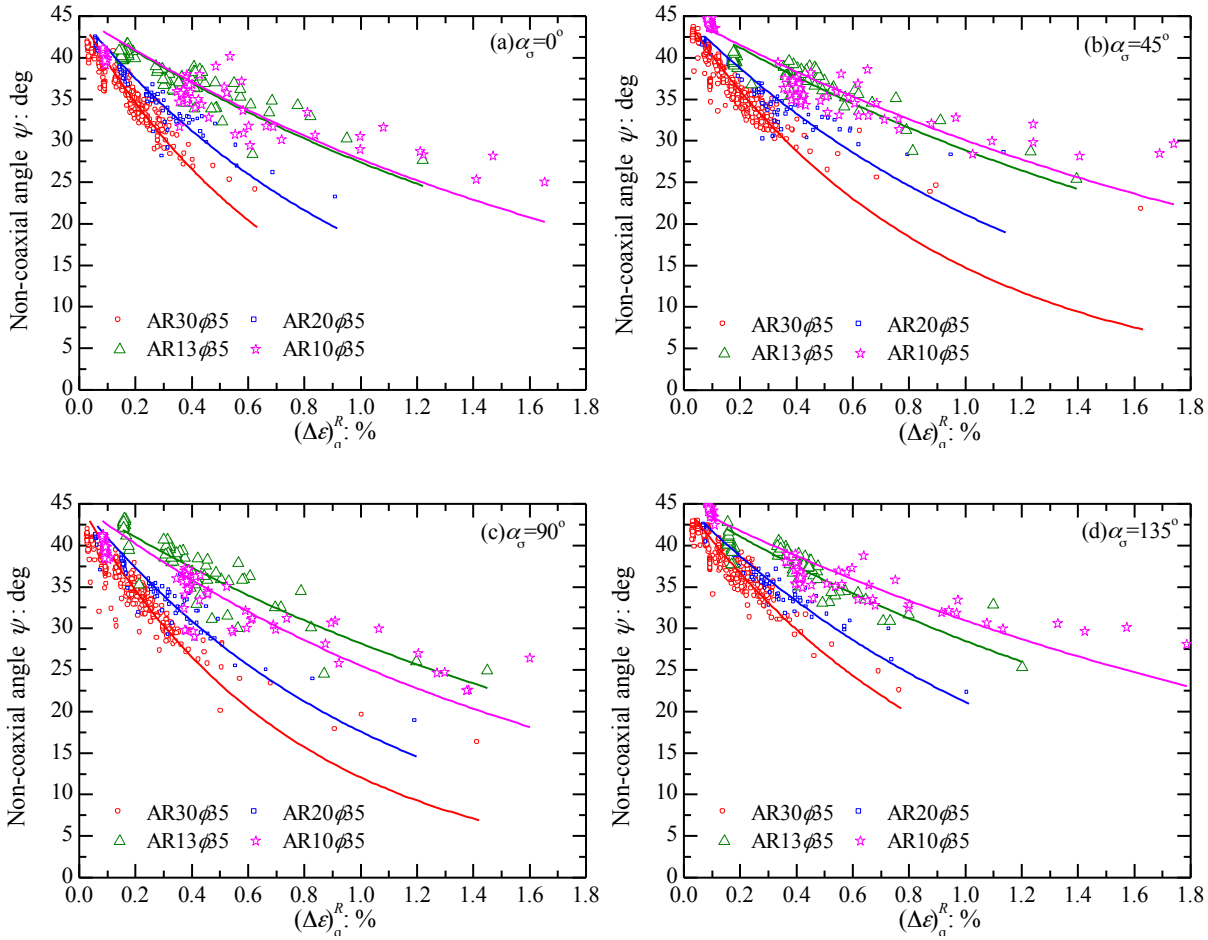

Figure 23 Effects of particle aspect ratio on the relationship between ψ and $(\Delta\varepsilon)_q^R$.

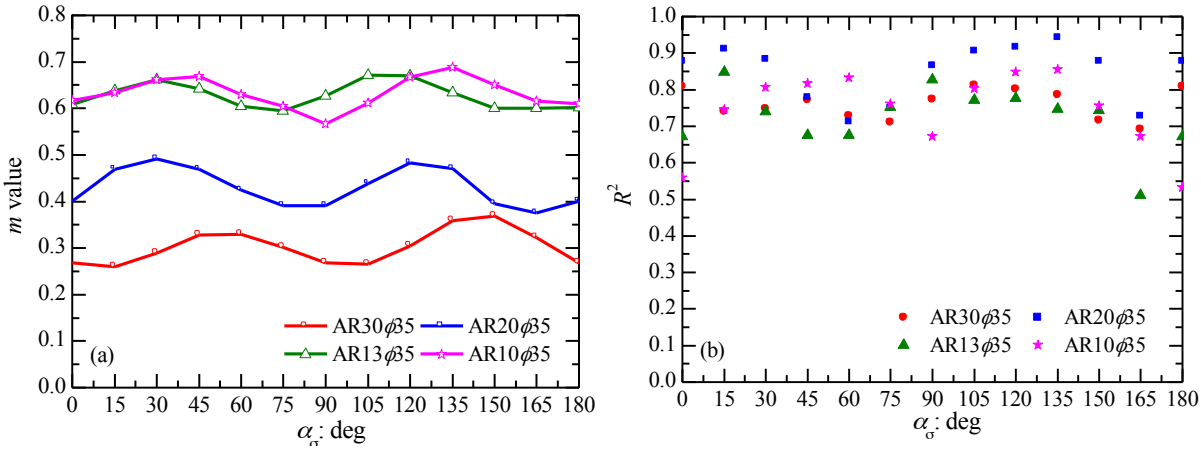

Figure 24 Effects of particle aspect ratio on variation of: (a) m value; and (b) R^2.

5 Concluding Remarks

This paper investigates the non-coaxial flow behavior of the cohesionless soil undergoing cyclic rotational shear, with a special interest in the effects of particle-scale characteristics, including particle elongation and inter-particle coefficient of friction. The "virtual material" studied is assemblies of discrete element particles. Such virtual material enables independent and precise control of particle-scale characteristics. Findings and conclusions are summarized as follows.

A large portion of the current paper is devoted to a comprehensive comparison between numerical simulation results for the virtual material and laboratory testing results for real world materials available in the literature. We found that the virtual material and real sands, both under rotational shear, share similar mechanical behaviors in many aspects, such as 1) general stress-strain behavior, 2) both the progressive development of contractive volumetric strain and the periodical variation of volumetric strain, and 3) the effects of stress ratio on the non-coaxial angle. The fact that the numerical simulation results are consistent with known laboratory testing results provides a great confidence in the validity of the previously unknown behaviors revealed by the numerical model. This observation lays a solid foundation for our subsequent research on related subjects beyond the current study.

We use two variables, the deviatoric part of the normalized strain increment and the non-coaxial angle in regards to stress, denoted by $(\Delta\varepsilon)_{\mathrm{q}}^{R}$ and ψ respectively, to quantify the flow behavior. The results show that $(\Delta\varepsilon)_{\mathrm{q}}^{R}$ decreases and ψ increases as the rotational shearing progresses. Both $(\Delta\varepsilon)_{\mathrm{q}}^{R}$ and ψ tend to approach a 'steady' or 'semi-steady' state.

We discover a strong yet simple relationship between ψ and $(\Delta\varepsilon)_{\mathrm{q}}^{R}$, which is independent of applied stress ratio, initial and current void ratio, and the number of cycles applied, but dependent on the principal stress orientation and particle-scale characteristics. At the same $(\Delta\varepsilon)_{\mathrm{q}}^{R}$, specimens with higher inter-particle friction angle or smaller particle aspect ratio show greater non-coaxial angles. A simple model $\psi = 45^{\circ} m^{(\Delta\varepsilon)_{\mathrm{q}}^{R}}$ is able to fit this ψ - $(\Delta\varepsilon)_{\mathrm{q}}^{R}$ relationship well. The parameter m is a function of inter-particle

friction angle, particle aspect ratio, and the orientation of the current principal stress direction with respect to the bedding plane when the incremental rotation of stress takes place. This simple model provides a useful relationship that can be explored and exploited in developing constitutive models for rotational shearing.

Acknowledgments

This work was made possible through extensive international collaboration. Tong and Yao's work was supported by National Basic Research Program of China (973 Program) (contract number 2014CB047006), Beijing Natural Science Foundation (contract number 8133053) and the National Natural Science Foundation of China (contract number 10902005 and 51079075). Fu's work was partly performed under the auspices of the U.S. Department of Energy by Lawrence Livermore National Laboratory under Contract DE-AC52-07NA27344 (LLNL release number: LLNL-JRNL-XXXXX). Y. F. Dafalias acknowledges support by the European Research Council under the European Union's Seventh Framework Program (FP7/2007-2013) / ERC IDEAS Advanced Grant Agreement n° 290963 (SOMEF) and partial support by the US NSF project CMMI-1162096.

References:

1. Ishihara K, Towhata K. Sand response to cyclic rotation of principal stress directions as induced by wave loads. *Soils and Foundations* 1983; 23(4): 11-26.
2. Wang ZL, Dafalias YF, Shen CK. Bounding surface hypoplasticity model for sand. *Journal of Engineering Mechanics* 1990; 116(5): 983-1001.
3. Miura K, Miura S, Toki S. Deformation behavior of anisotropic sand under principal stress axes rotation. *Soils and Foundations* 1986; 26(1): 36-52.
4. Symes MJ, Gens A, Hight DW. Drained principal stress rotation in saturated sand. *Geotechnique* 1988; 38(1): 59-81.
5. Vaid YP, Sayao A, Hou EH, Negussey D. Generalized stress path dependent soil behavior with a new hollow cylinder torsional apparatus. *Canadian Geotechnical Journal* 1990; 27: 601-616.
6. Wijewickreme D, Vaid YP. Behavior of loose sand under simultaneous increase in stress ratio and principal stress rotation. *Canadian Geotechnical Journal* 1993; 30: 953-964.
7. Zhang JM, Tong ZX, Yu YL, Zhang G. Effects of cyclic rotation of principal stress axes and intermediate principal stress parameter on the deformation behavior of sands. *GEESD IV*, New York, D. Zeng, M. Manzari, and D. Hiltunen, eds., *ASCE Geotechnical Special Publication*, 2008; 181.
8. Tong ZX, Zhang JM, Yu YL, Zhang G. Drained deformation behavior of anisotropic sands during cyclic rotation of principal stress axes. *Journal of Geotechnical and Geoenvironmental Engineering* 2010; 136(11): 1509-1518.
9. Ishihara K, Yamazaki A. Analysis of wave-induced liquefaction in seabed deposits of sand. *Soils and Foundations* 1984; 24(3): 85-100.

10. Symes MJ, Gens A, Hight DW. Undrained anisotropy and principal stress rotation in saturated sand. *Geotechnique* 1984; 34(1): 11-27.

11. Towhata I，Ishihara K. Undrained strength of sand undergoing cyclic rotation of principal stress axes. *Soils and Foundations* 1985; 25(2): 135-147.

12. Nakata Y, Hyodo M, Murata H, Yasufuku N. Flow deformation of sands subjected to principal stress rotation. *Soils and Foundations* 1998; 38(2): 115-128.

13. Yang ZX, Li XS, Yang J. Undrained anisotropy and rotational shear in granular soil. *Geotechnique* 2007; 57(4): 371-384.

14. Roscoe KH, Bassett RH, Cole ER. Principal axes observed during simple shear of a sand. *Proc. Geotech. Conf., Oslo* 1967; 1: 231-237.

15. Wong RKS, Arthur JRF. Sand sheared by stresses with cyclic variations in direction. *Geotechnique* 1986; 36(2): 215-226.

16. Hong WP, Lade PV. Strain increment and stress directions in torsion shear tests. *Journal of Geotechnical Engineering* 1989; 115(10): 1388-1401.

17. Pradel D, Ishihara K, Gutierrez M. Yielding and flow of sand under principal stress axes rotation. *Soils and Foundations* 1990; 30(1): 87-99.

18. Gutierrez M, Ishihara K, Towhata I. Flow theory for sand during rotation of principal stress direction. *Soils and Foundations* 1991; 31(4): 121-132.

19. Cai Y, Yu HS, Wanatowski D, Li X. Noncoaxial behavior of sand under various stress paths. *Journal of Geotechnical and Geoenvironmental Engineering* 2013; 139(8): 1381-1395.

20. Yin ZY, Chang CS, Hicher PY. Micromechanical modelling for effect of inherent anisotropy on cyclic behaviour of sand. *International Journal of Solids and Structures* 2010; 47(14-15): 1933-1951.

21. Fu P, Dafalias YF. Fabric evolution within shear bands of granular materials and its relation to critical state theory. *International Journal for Numerical and Analytical Methods in Geomechanics* 2011; 35(18): 1918-1948.

22. Li XS, Dafalias YF. Anisotropic Critical State Theory: Role of Fabric. *Journal of Engineering Mechanics* 2012; 138(3): 263-275.

23. Cundall PA, Strack ODL. Discrete numerical model for granular assemblies. *Geotechnique* 1979; 29(1): 47-65.

24. Thornton C. Numerical simulations of deviatoric shear deformation of granular media. *Geotechnique* 2000; 50(1): 45-53.

25. Ng TT. Shear strength of assemblies of ellipsoidal particles. *Geotechnique* 2004; 54(10): 659-669.

26. Cui L, O'Sullivan C, O'Neill S. An analysis of the triaxial apparatus using a mixed boundary three-dimensional discrete element model. *Geotechnique* 2007; 57(10): 831-844.

27. Fu P, Dafalias YF. Study of anisotropic shear strength of granular materials using DEM simulation. *International Journal for Numerical and Analytical Methods in Geomechanics* 2011; 35(10): 1098-1126.

28. Masson S, Martinez J. Micromechanical analysis of the shear behavior of a granular material. *Journal of Engineering Mechanics* 2001; 127(10): 1007-1016.

29. Cui L, O'Sullivan C. Exploring the macro- and microscale response characteristics of an idealized granular material in the direct shear apparatus. *Geotechnique* 2006; 56(7): 455-468.

30. Zhang L, Thornton C. A numerical examination of the direct shear test. *Geotechnique* 2007; 57(4): 343-354.

31. Li X, Yu HS. Numerical investigation of granular material behavior under rotational shear. *Geotechnique* 2010; 60(5): 381-394.

32. Fu P, Walton OR, Harvey JT. Polyarc discrete element for efficiently simulating arbitrarily shaped 2D particles. *International Journal for Numerical Methods in Engineering* 2011; 89(5): 599-617.

33. Krishnasamy J, Jakiela MJ. A method to resolve ambiguities in corner-corner interactions between polygons in the context of motion simulations. *Engineering Computations* 1995; 12(2): 135-144.

34. Mirghasemi AA, Rothenburg L, Matyas EL. Numerical simulations of assemblies of two dimensional polygon shaped particles and effects of confining pressure on shear strength. *Soils and Foundations* 1997; 37(3): 43-52.

35. Nouguier-Lehon C, Cambou B, Vincens E. Influence of particle shape and angularity on the behaviour of granular materials: a numerical analysis. *International Journal for Numerical and Analytical Methods in Geomechanics* 2003; 27(14): 1207-1226.

36. Han K, Feng YT, Owen DRJ. Polygon-based contact resolution for superquadrics. *International Journal for Numerical Methods in Engineering* 2006; 66: 485-501.

37. Rosin PL. A survey and comparison of traditional piecewise circular approximations to the ellipse. Computer Aided Geometric Design 1999; 16(4): 269-286.

38. Fu P, Dafalias YF. Quantification of large and localized deformation in granular materials. *International Journal of Solids and Structures* 2012; 49: 1741-1752.

39. Tong ZX, Zhang LW, Zhou M. DEM simulation of biaxial compression experiments of inherently anisotropic granular materials and the boundary effects. *Journal of Applied Mathematics*, 2013.

40. Tong ZX, Fu P, Zhou SP, Dafalias YF. Experimental investigation of shear strength of sands with inherent fabric anisotropy. *Acta Geotechnica* 2014, DOI: 10.1007/s11440-014-0303-6.